London Centre of Nanotechnology
University College London
University of London

Neutron Pair Distribution Function Analysis and 3D Modelling: Structural Investigation of FePt Nanoparticle-Ligand Systems

Marianne Monteforte

Supervisor: Ian K. Robinson
Secondary Supervisor: Jeremy Cockcroft

Submitted in partial fulfilment of the requirements
for the degree of MPhil
at the University of London

January 30, 2013

Contents

List of Figures

Abstract

FePt nanoparticles (NPs) are a diverse class of magnetic NPs, which exhibit attractive properties for potential applications, from high density data storage devices to biomedical applications. The physical properties of FePt NPs are also of specific interest for these applications, as they have an order of one magnitude larger magneto-crystalline anisotropy (K_u= Ca. $7x10^7 erg/cm^3$) compared to competitor magnetic NP candidates of FeO, and CoCr [Rong et al., 2010].

FePt NPs have been reported to have a size range of 1.5 - 35 nm (15 -350 Å) depending on the parameters of the synthesis method. The experimental top-down method,wet chemical synthesis of spherical equiatomic FePt NPs, of diameter $<$ 50 Å(5 nm), has been successfully synthesised at the Davy-Faraday Research Laboratory at the Royal Institution. This standard synthesis procedure involves an alleo-catalytic thermal decomposition reaction of the dual-source metal precursors of Fe and Pt in the presence of stabilising surfactants, oleic acid and hexadecylamine, and a high temperature reaction solvent. The as-synthesized FePt NPs have a chemically disordered fcc structure and are super-paramagnetic at room temperature. The synthesis and chemical properties of these fcc NPs have been extensively reported, however very few experimental investigations of this kind have been reported to date. Therefore, the investigation herein, aims to determine the internal structure and morphology of these binary alloy NPs and to determine the structural parameters, speciation and properties of the surfactant layer, surrounding these NPs. The advanced analysis technique of Pair Distribution Function (PDF) is applied to both x-ray and neutron total scattering diffraction data of the NP systems providing quantitative real space information about both the inter-atomic bonding in the NP and intra-atomic bonding of the NP with the surfactant layer.

The **Internal Structure of the FePt Alloy NP** is of fundamental interest. The competing ordering of the bulk phases and surface segregation, not to mention magnetic ordering, is expected to lead to a complex variety of structures for such particles, which are entirely unknown. The FePt phase diagram is rich in ordered phases and considered a classic example of a binary alloy, with a large literature. Nanoscale binary alloys are expected to be very different from bulk because surface segregation effects are large and can dominate the structure. Segregation can also lead to core-shell structures with interesting compositional modulations strongly coupled to the morphology. There have been few investigations that have fully determined the relationship between size, segregation, magnetic ordering, composition of these NP alloys.

The surrounding **Acid and Amine Capping Surfactants** facilitate the formation of the NP, and stabilises the NPs in their solvent dispersion, preventing aggregation. It has been hypothesised, but not yet demonstrated, that the Fe atoms on the surface of the NP are specifically associated with the carbonyl group of the surfactant through Fe-O bonds, while the Pt atoms are associated with the amine group of the other surfactant via $Pt - NH_2$ bonds. The interaction of the NP with the functional group of the ligand often critically affects its properties and, in turn the performance, yet there is little known about the way surfactants bind and interact with particle surfaces. The outcome of the investigation, is to not only advance this field of research, but also enable the NPs physical properties to be enhanced and their ligand exchange ratios to be defined allowing for the function of the NP and surfactant to be utilised effectively.

The **Pair Distribution Function** is measured experimentally by applying a reverse Fourier

Transform to high energy x-ray/neutron diffraction patterns and provides a complete structural fingerprint of a system in real space. This PDF analysis technique, traditionally has been used to overcome the difficulties in characterising the atomic scale structure of disordered crystalline materials, liquids and amorphous systems [Egami and Billinge, 2003]. Only recently, over the past decade have the tools emerged for the application of this technique to be extended in order to analyse powder NP systems.

The results of the experimental synthesis and analysis of FePt NPs with hydrogenated surfactants for x-ray and neutron PDF analysis are presented herein.

The **XRD-PDF Results** acquired from ISIS Ag $^{+}K_{alpha}$ laboratory source x-ray diffractometer validate the sensitivity of the PDF technique. Data processing of the normalised diffraction data was carried out using the GudRunX program to give the corresponding pair distribution function (PDF) of the data. The size of the NP, and interatomic bond lengths correlated with the results from TEM size analysis and the theoretical bond length values. Quantitative analysis of the PDF revealed interatomic bond lengths of fcc FePt which correlated well the theoretical bond length values. Also, the PDF yields a NP size of 40 Å(4 nm), in good agreement with the size obtained from the TEM images. The results obtained from the XRD-PDF confirms that the PDF technique applied to powder diffraction patterns of FePt NPs is effective and allows for the continuation of the application of this technique to diffraction patterns obtained from neutron diffraction measurements.

The **Neutron Diffraction-PDF Measurements**, were carried out utilising the Near Intermediate Range Order Diffraction beamline, (Nimrod) at ISIS. The Near Intermediate Range Order beamline, Nimrod consists of a wide range of detectors with continuous Q range from 0.01 $Å^{-1}$ to 50 $Å^{-1}$, that bridges the gap between small angle and wide-angle neutron scattering [Bowron et al., 2010]. It is intended to take advantage of this, for effective analysis of the whole NP system, from the surrounding atom-atom surfactant to the shortest internal correlations. Two samples of FePt NPs were analysed; one of which was synthesised with the standard hydrogenated surfactant and the other that was synthesised with deuterated surfactant. The differences in the PDF acquired from the FePt NPs with hydrogenated surfactant, and the FePt NPs with par-deuterated surfactant, demonstrated the pronounced benefit of probing the structure of the surfactant using isotopic substitutions. Also, in this resultant PDF of the NP-surfactant system, structural information from the surfactant was identifiable before the first nearest neighbour peak of the NP which is a step forward in proving the bonding hypothesis. Close inspection of the central r-range, 2-6 Å, of the PDFs enabled the 1st, 2nd and 3rd nearest neighbour bonds in the FePt NP to be asigned to the peaks with the closest match to those obtained from the model FePt NP .

An advanced PDF nanostructure **Modelling Package, DIFFUSE,** was used to model a NP of a range of sizes and internal arrangements. The resultant calculated PDFs of these models were then compared to the PDF of the observed data set, and refined to create a model NP with an internal structure with the closest representative to the NP analysed. The 3D NP models were created with the instrumental parameters defined within the PDF macros in order to obtain a model that was the closest representation of the NPs that were analysed in the neutron diffraction measurements. The results from the calculated PDFs of the 3D models of 20Åand 40Åspherical NPs demonstrated the size effects of the NP on the PDF. Randomly

disordered structures of FePt NPs were successfully modelled and NN distances and surface sites for future ligand attachment were identified. Core-shell structures (FePt@Pt) of FePt NPs were also successfully modelled. At the time of print NPs of SRO were in the process of being modelled. Determining the effect that the atomic structural arrangement in a NP have on the PDF model is part of this ongoing investigation. Complementary high energy XRD data was obtained from Sample AM01, 20ÅFePt NPs in collaboration with Valeri Petkov, and a 3D model and calculated PDF was created on the basis of the experimental data acquired.

On completion of the data analysis and ongoing work outlined within, the results are expected to shed new light on the fundamental properties of NPs, notably the compositional variations within nanoscale alloys, and enable key applications in medicine and information technologies.

Chapter 1

Background

1.1 Unique Properties of Nanoparticles

In 1857 Michael Faraday pioneered the production of an aqueous suspension of metal NPs (colloidal gold, using a two phase reduction method [Turkevich J, 1951]), identifying the unique properties of NPs. This paved the way in the field of NP synthesis and analysis for implementation of the advanced progression of the applications discussed within. NPs are a leading class of magnetic materials and exhibit properties in the scope between bulk materials and individual atoms. They present unique chemical, physical, and electronic properties with respect to the bulk, due to surface atom effects coming into play [Luo et al., 2006]. As the surface to volume ratio increases with decreasing NP size, the behaviour of small NPs becomes increasingly influenced by their surface properties. An average of 20% of atoms with respect to the core, contribute to the surface of the NP. This accessible surface for surfactant attachment is of particular interest, in order to develop the functionality of the NP. The FePt NP surface has a strong binding affinity towards acid and amine groups, and their functionality can be tailored through exchanging surfactants with particular ligands. The exchange allows for surface conjugation, via the ligand, with various peptides, proteins, antibodies and other biomolecules. NPs are therefore readily amenable to bio-conjugation and bio-modification.

1.2 Proposed Nanoparticle Formation

Today, bimetallic NP alloys can be synthesised via either bottom-up or top-down methods. The bottom-up, physical, method is where the metal ions that are produced from corresponding metal atoms are directed through a heated reaction changer onto a substrate to form a controlled aggregation of the metal NP alloy, whereby the temperature controls the size produced [Chen et al., 2007]. The top-down, chemical, method is where the metal NP alloy is synthesised under inert conditions, and the corresponding metal salts are reduced in solution to bimetallic NPs in the presence of stabilising surfactants. This approach was adopted in the standard synthesis procedure of the FePt NPs, and involves an alleo-catalytic thermal decomposition reaction of the dual-source metal precursors of Fe and Pt, in the presence of stabilising acid and amine

surfactants, and a high temperature reaction solvent [Sun, 2006]. The size and geometry of the NPs was controlled by adjusting the chemical reaction parameters.

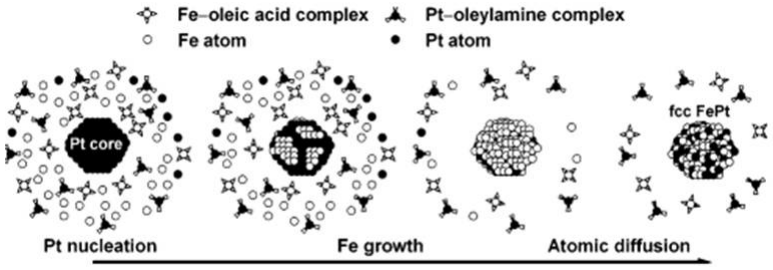

Figure 1.1: *Schematic of postulated FePt formation mechanism with initial nucleation of the Pt 'seed', Fe growth on surface and final stage atomic diffusion of Fe, where the thermodynamic force drives the Fe atoms from the surface to the core of a Pt 'seed' cluster forming FePt [Saita and Maenosono, 2005]*

It is postulated that initial decomposition of the Fe precursor acts as a catalyst for the decomposition of the Pt precursor [Saita and Maenosono, 2005]. The reaction formation mechanism in Figure1.1 is suggested to follow an initial nucleation of Pt and a slow growth of Fe via alleocatalytic decomposition. The formation mechanism during the synthesis itself is expected to to define the internal arrangement of the NP. Previous reports have shown that NPs of monodisperse distribution and equi-atomic composition can be synthesised through tailoring of this method.

1.3 Potential Applications of FePt NPs

NP investigations are the subject of current scientific research, due to the wide variety of potential practical applications, primarily in the nanotechnical and biomedical fields. Typically, monodisperse NPs with a narrow size distribution are attractive candidates for the following applications, illustrated in Figure 1.2:

- **Information Storage**- For this application to perpendicular magnetic mediums it is required for the NPs to be monodisperse so that the NPs form a 2D self-assembled superlattice on a substrate. Each NP array consists of a perpendicular magnetic domain which can be magnetically manipulated, using a 'monopole' writing element, to retain data, [Saita and Maenosono, 2005c]. The ongoing endeavour to continue the bit size reduction for data storage beyond 1 $Tbit/in^2$, whilst maintaining a stable magnetisation, requires materials with high magneto-crystalline anisotropy such as the face centred tetragonal phase of FePt NPs.

- **Catalysis**- FePt@Pt core-shell NPs can act as catalytically active nano-magnets used for the oxygen reduction reaction in fuel cells, it is an excellent CO tolerant catalyst and Fe is much cheaper than its counterpart Cu, which has been previously used.

- **Targeted Drug Delivery** - The magnetic NP can be guided by a magnetic field onto the surface of a tumour of a patient and the attached biomolecule can enter the affected cell, through the cell wall.

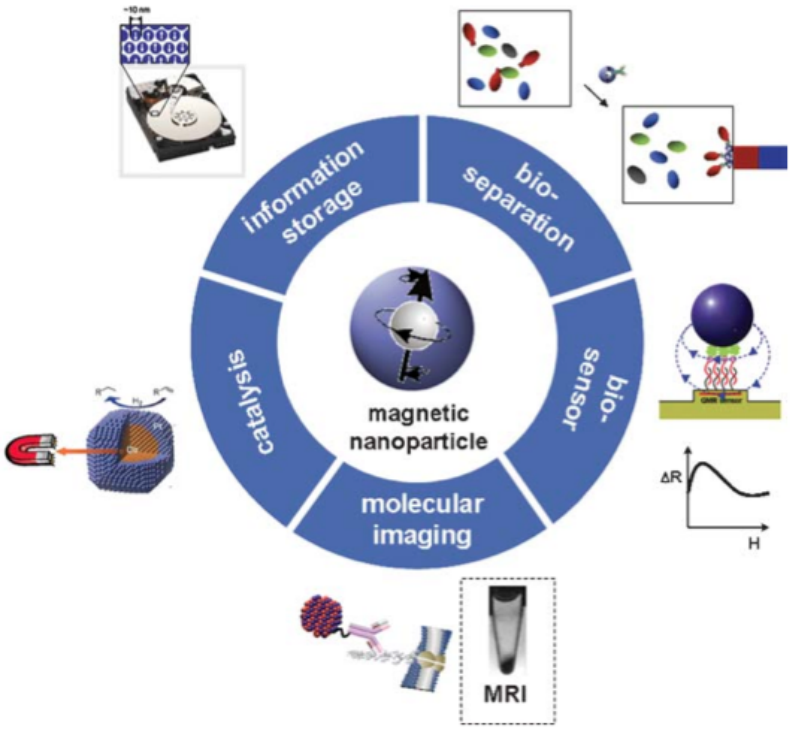

Figure 1.2: *Potential applications of magnetic nanoparticles for high performance nanosystems [Jun et al., 2007]*

- **Bioseperation**- NPs can be tagged with a specific ligand and then bound to a system for segregation through the use of magnets.
- **Molecular Resonance Imaging** - NPs act as high contrast agents enabling the movement of the NP in the system to be tracked, due to the strong magnetic coercivity of FePt.
- **Hyperthermia** - Magnetic hyperthermia for cancer therapy is where the NP targets an isolated tumour, entering through the cell wall. The NP is then exposed to an a.c magnetic field,which results in magnetic spin flipping of the magnetically active NP, causing a radio frequency induced heat destruction of the cell [Hergt et al., 2006].

1.4 Nanoparticle Internal Structure

1.4.1 FePt Nanoparticle Phases

There exist two main phases of FePt NPs: disordered face-centered cubic (fcc), A1 phase, at room temperature; and ordered face centered tetragonal (fct), $L1_0$ phase on heat transformation. The phase transformation from fcc to fct occurs on annealing in an inert environment at temperatures above $400°C$, resulting in a small tetragonal compression of the c-axis along the (001) plane of the unit cell, which in turn causes a change in lattice parameter ratio c:a. Full conversion into the fct phase requires the stoichiometry Fe_xPt_{1-x} to be within the range

of $0.4 > x > 0.6$ [Nguyen et al., 2006]. An intermediate, $L1_2$ phase exists, with a compositionally ordered body-centered cubic (bcc) structure, can become present on annealing when the composition is out with the given stoichiometric range.

1.4.2 Morphology

The as-synthesised NPs, are postulated to exhibit either a disordered, short-range order or core-shell structural arrangement of Fe and Pt atom as in Figure 1.3 a). Such a coreshell structure of FePt@Pt or FePt@Fe, is disadvantageous in view of the subsequent transformation into the more commercially desired $L1_0$ phase. Based on theoretical calculations, it can be expected that, for core-shell structures, a higher amount of thermal energy is required for the phase transition, than for randomly orientated structures, and that a lower degree of ordering per particle is obtained [Saita and Maenosono, 2005]. On phase transformation into fct, the Fe and Pt atoms are stacked

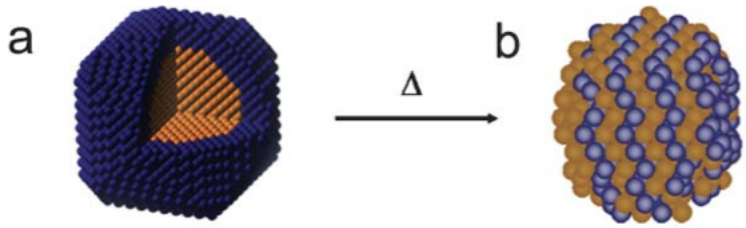

Figure 1.3: *a)Core-shell model, requires a greater thermal energy to transform into b) ordered fct phase than an as-prepared randomly disordered NP*

in layers sequentially along the c-axis, (001) plane. The significance of the fct phase is that it exhibits magnetic properties due to the distinct Pt and Fe layering, resulting in strong spin orbit coupling, enhanced coercivity along c, and a high magneto-crystalline anisotropy (large enough to thermally stabilise the magnetisation of NPs as small as 3.5 nm) [Delalande et al., 2012].

1.4.3 Nanoparticle Composition

The morphology, size and composition which influences this arrangement is based on the most energetically stable state. For example, icosahedral of size 5-6 nm, with a near equiatomic composition, $Fe_{52}Pt_{48}$, are expected to exhibit an energetically favoured core-shell structure with Fe rich core, $Fe_{80}Pt_{20}$, and a Pt rich shell. Whereas, NPs which exhibit a non-stoichiometric composition, $Fe_{25}Pt_{75}$, have been shown to systematically lead to NPs with an Fe-depleted core and an Fe-rich shell [Saita and Maenosono, 2005]. However, these incidences are not directly comparable due to the use of dodecanitrile, in the report by Wang et. al, in place of the standard olelyamine surfactant. The cyanide group of the dodecanitrile binds more strongly to the Pt than the amine group of the oleylamine, during the synthesis reaction, thus preventing the nucleation of the Pt. This is postulated to result in a more stoichiometric composition. This demonstrates the complexity of the type of surfactant, with different functional groups, used during the synthesis and its contribution to the resultant internal arrangement of Fe and Pt.

1.4.4 Magnetic Properties

The $L1_0$ phase, exhibits ferromagnetic behaviour at room temperature, and, on applying an external magnetic field, the $L1_0$ phase will act as a hard magnet, retaining some of the magnetism even when the magnetic field has been removed - a property known as remanance. Whereas the A1 and $L1_2$ phases exhibit superparamagnetic behaviour and will act as a soft magnet, only exhibiting remanance at very low temperatures. The $L1_2$ phase has similar cell parameters (a, b = 3.905 Åand c = 3.735 Å) to the A1 phase, and the $L1_2$ phase (a = b = c= 3.872 Å). These different phases have unique planes which are customarily identified by powder X-ray diffraction.

1.5 Surfactant Layer

Surfactants are usually amphiphilic organic compounds, with an ionic head such as NH^{2+} and COO^{-}, in this case of the amine and acid surfactants. Surfactants are a vital component in the synthesis of NPs, as they control the particle growth of the preliminary formed NPs. The molar ratio of the acid:amine surfactant used in the synthesis has been suggested to play a role in the resultant size, structure and morphology of the NP. The surfactants attach to the interface of a plane restricting the growth of specific planes to which they bond. In this investigation the ratio of amine:acid surfactant is set at 1:1 which results in the NP planes growing at the same rate, forming a spherical NP. Furthermore, the surfactants continue to act as stabilising agents to the as-synthesised NPs in colloidal solution, preventing aggregation of the suspended NPs and influence the self-assembly of the NPs on a substrate.

1.5.1 Amine Surfactant

Oleylamine (OLA) is the standard surfactant that is used in accordance with OA. However in this investigation OLA be substituted by Hexadecylamine (HDA) as it is more readily available in deuterated form and has been used in other reports [Nguyen et al., 2006]. The HDA, $C_{16}H_{35}N$, only varies from OLA,$C_{18}H_{37}N$,by two carbon chain lengths resulting in the decomposition temperature of HDA, b.p = 330°C, being slightly lower than that of OLA, b.p = 348°C. The chemical properties of the two amines are similar, and therefore it is expected that this change of surfactant will not affect the resultant NPs. The extended chain length of HDA is 2.18 nm [van Ewijk et al., 2002].

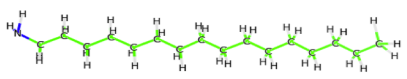

Figure 1.4: *Structure of HDA created using pymol*

1.5.2 Acid Surfactant

Oleic acid (OA),is a surfactant with an extended chain length of 2.08 nm [van Ewijk et al., 2002] which bonds via a dentate/bidentate bond to the Fe. OA $C_{18}H_{34}O_2$, exhibits two isomer forms due to orientation of the central carbon double bond resulting in the trans-OA straight molecule form and the cis-OA of bent molecule for as in Figure 1.5.

An FTIR study by Walburn et. al, on this isomerisation showed that the Fe^3+ catalyses the cis $\rightarrow$trans transformation by switching an electron from the cis double bond causing it to change from sp^2 hybridised to sp^3 hybridised REF walburn:2002 [A V Walburn et al., 2002]. The cis-form has been reported to be present when there is a high concentration of Fe present on the NP surface [Shukla et al., 2003]. Therefore if this is the case where Fe acts as the catalyst, then there will be no coupled hydration-dehydrogenation reaction on transformation. In the report by [J. Bacteriol., 2003] it was also proven by mass spectrometry that there was no loss of deuterium during the transformation which showed the shift of two a.m.u's.

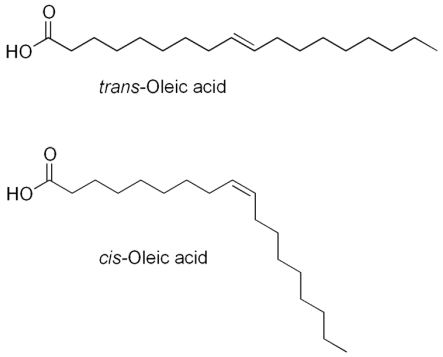

Figure 1.5: *Structure of trans-0A and cis-OA (Eladyl form)[Nisha Shukla et al, 2003]*

1.5.3 Surfactant Interaction

The interaction of the NP with the functional group of the ligand often critically affects its performance or resultant properties, yet there is little known about the way ligands bind and interact with particle surfaces. Accurate determination of atomic surface structure is essential in order to understand and utilise the function of the ligand effectively. It is only hypothesised, but not yet demonstrated, that the Fe atoms on the surface of the NP are specifically associated with the carbonyl group of the surfactant through Fe-O bonds, while the Pt atoms are associated with the amine group of the other surfactant via Pt-NH_2 bonds [Sun, 2006],[Suda et al., 2007], as illustrated in Figure1.6. It is expected also, that the acid and amine favour the growth of different facets of the fcc NP. If this hypothesis were proven, then the surfactants selective binding could effectively be considered as a probe in the analysis of the NP surface properties.

The surrounding surfactant layer is expected to be of a single layer of OA and HDA which would create an additional shell of extended length of 2.18 nm. However, it could be possible that there are additional shells of OA and HDA that have ionically bonded to the first surfactant layer, and this could be a profitable subject for future Pair Distribution Function analysis. The possibility that the acid and amine surfactant have bonded to form diolamide and interact with the [Calatayud et al., 2013].

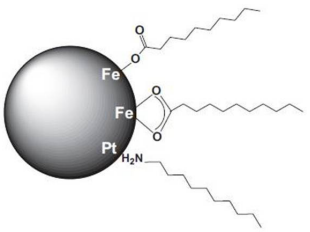

Figure 1.6: *FePt NP representing specific bonding behaviour of the acid and amine surfactant to Fe and Pt respectively*

Chapter 2

The Atomic Pair Distribution Function

The Atomic Pair Distribution Function (PDF), otherwise termed the radial distribution function, or pair correlation function, is a principally well understood method, the concept of which was initially described in the classical 1969 textbook, by Warren on X-ray diffraction [Addison Wesley; New-York, Dover]. A reverse Fourier Transform equation is applied to the powder diffraction data to give the real-space PDF. This analysis technique traditionally has been used to overcome the difficulties in characterising the atomic scale structure of disordered crystalline materials, liquids and amorphous systems [Egami and Billinge, 2003]. Only recently, over the past decade, have the tools and software capabilities emerged for the application of this technique to be extended in order to analyse powder NP systems [Korsounski et al., 2003; Gilbert et al., 2004; Page et al., 2004, 2010; Neder and Korsunskiy, 2005; Pradhan et al., 2007; Billinge and Levin, 2007; Masadeh et al., 2007; Chupas et al., 2007].

2.1 Total Scattering

The PDF analysis technique accounts for both **Bragg** and **Diffuse** scattering components obtained from the diffraction pattern. The Bragg component provides information on the average structure, assuming periodicity, and is effectively 'blind' to the local co-ordination environment of the atoms in NP systems. This is where the diffuse component comes into play; it effectively accounts for this missing information due to local deviations from the average structure. This diffuse scattering is manifested beneath and between the Bragg peaks, and in conventional structural analysis of diffraction patterns it is subtracted as background [Young and Goodwin, 2011]. The PDF is applied to the whole diffraction pattern containing the **Total Scattering**, and made up of both the Bragg and Diffuse components, and therefore enables the determination of structural information about the whole system, from the long range atomic structure to the local imperfections, e.g chemical short range order.

2.2 Theory of Pair Distribution Functions

2.2.1 Scattering Vector, Q

The scattering vector Q, is the resultant wave vector change in the scattering, and is defined as $Q = k_i - k_f$, where k_i is the initial wavevector and k_f is the final wavevector. This resultant wave vector,Q, can be calculated in terms of angle in Eq 2.1 for elastic scattering, where 2θ is the diffraction angle and λ is the radiation wavelength:

$$Q = \frac{2\pi sin.2\theta}{\lambda} = \frac{2\pi}{d} \tag{2.1}$$

In order to obtain maximum resolution and minimise the termination ripples due to the Fourier Transform, experimental PDFs require diffraction data of high statistical value and high Q_{max}. High-energy x-ray synchrotron and spallation neutron sources are routinely used for this purpose due to their short λ.

2.3 PDF Equation

The PDF, G(r),is defined as the relative probability of finding another atom in a unit volume at a distance, $\vec{r}$ from the reference atom. G(r) is outlined in Eq. 2.2, where $\rho(r)$ is the instantaneous pair density at $\vec{r}$ and ρ_0 is the average number density.

$$G(r) = 4\pi r[\rho(r) - \rho_o] \tag{2.2}$$

$$G(r) = 4\pi\rho r[\rho(\vec{r}) - \rho_0\vec{]}) \tag{2.3}$$

$$G(r) = (2/\pi) \int_{Q=0}^{Q_{max}} Q[S(Q) - 1] \sin(Qr)\, dQ \tag{2.4}$$

The PDF is generated from the sine Fourier transform of the normalised total scattering diffraction data as in Eq. 2.4), where Q is the scattering vector (described below) and Q[S(Q)-1] is the normalised total scattering data. The diffraction data in the PDF differs in terms of the radiation type used, as x-rays and neutrons have different structure factors - I(Q) and S(Q), respectively. The integration range is theoretically defined over the limits over all space ($0 \rightarrow \infty$), but practically the limit is: $Q_{min} \rightarrow Q_{max}$ where the lower limit Q_{min}, is restricted by the effects of direct beam, and set at 0 and the upper limit Q_{max} is restricted by the wavelength (λ) of the radiation. A high Q_{max} is needed to resolve coordination peaks at similar distances.

2.3.0.1 Diffraction Pattern Analysis

The Bragg peaks in a diffraction pattern correspond to the quantitative phase fractions and unit cell lengths of the NP system. The peak positions correspond to the angle of diffraction, and therefore the d-spacings (inter planar spacing) enabling individual NP planes to be identified. From analysis of the peak shape and the width the crystallite size of the NP can be determined through application of the Scherrer equation. In general, as the diffraction is in reciprocal space, the size of the peak width varies inversely with crystallite size. Also, on analysis of the normalised diffraction patterns with intensity vs. S(Q), as Q = 2π/d then the d space values can be calculated.

Atoms in the same plane will result in constructive interference and will satisfy Bragg's Law (n = 2dsin θ). Each phase has certain allowed reflections in accordance with the selection rules. The section rule for a cubic system is detailed in Eq 2.5, where d is the inter planar spacing, a is the size of the unit cell and h,k,l are the miller indices for different cubic Bravais lattices. The allowed reflections for a face-centered cubic system are all even or all odd h,k,l and the forbidden reflections are mixed odd and even h,k,l.

$$d = \frac{a}{\sqrt{h^2 + k^2 + l^2}} \tag{2.5}$$

Thus, the characteristic planes in fcc FePt NPs are at (111),(200), (220) (where the (111) lattice spacing of fcc FePt has been stated to be 0.235 nm [Rong et al., 2006]). Additional planes of fcc are (311) and (333).

2.4 PDF Analogy

Figure 2.1 demonstrates a 2D Analogy of a PDF system where the peaks corresponds to quantitative atomic distances,r, from an atom at the reference point of origin; 1st peak is the first nearest neighbour ,NN,the 2nd peak is the second NN and so forth. The following information can be extracted from the PDF data:

- The first r value gives the cut-off value (lowest possible resolution)
- The peak height corresponds to the co-ordination number,and determines the average number of NNs e.g. 5 could be an average of atoms with 4-fold and 6-fold co-ordination
- The peak width corresponds to the dynamic vibrations between atoms
- The point where the peaks diminish ('termination ripples') corresponds to the largest possible bond distance within the NP, thus represents the diameter of the NP. This 'cut-off point' is where Q=Q_{max}

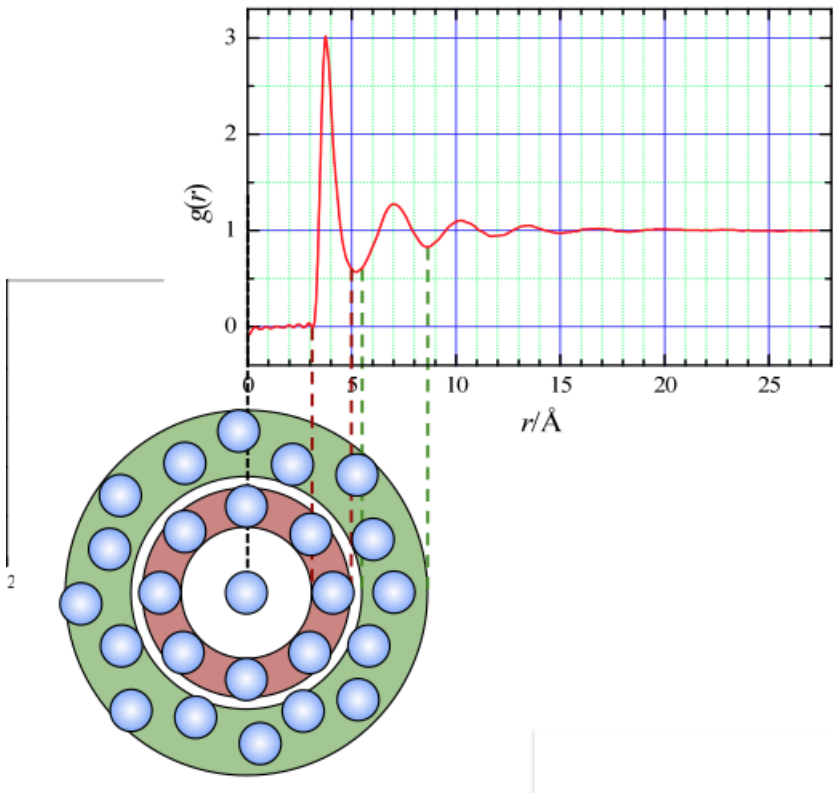

Figure 2.1: *Analogy of an example PDF system where the peaks corresponds to interatomic distances in real space [Gabriel Cuello, 2012]*

2.5 Why choose Neutrons as the Radiation Source?

2.6 X-rays vs. Neutrons

X-rays and neutrons interact with matter differently, due to their different properties;

X-rays are electromagnetic waves ('packets of photons') which have spin +1 and no magnetic dipole moment. X-rays interact primarily with the surrounding electron cloud of the atom, resulting in the scattering power of an atom dropping off with scattering angle, as illustrated in the plot and corresponding schematic in Figure. 2.2 a). The scattering power, f(q), is proportional to atomic number, Z. Only when the scattering angle is equal, $2\theta = 0°$, is f (q) = Z, e.g H^1 has only one electron so the scattering off the electron cloud is weak as the f(Q) = 1.

Neutrons are fundamental neutrally charged particles which exhibit particle-wave duality, with a spin of +1/2 and an intrinsic magnetic dipole moment. This magnetic moment interacts with the spin of unpaired electrons of an atom, and can also be utilised for magnetic scattering measurements. Neutrons interact via the short range nuclear force, primarily with the nuclei of the atom. The scattering power is independent of the scattering angle, 2 θ, as illustrated in the plot and corresponding schematic in Figure 2.2 b),and therefore independent of Z.

Neutrons can be used to detect light elements such as H (Z = 1) and Fe (Z = 26) in the presence of heavy elements, e.g Pt (Z = 78), these are difficult to distinguish between using x-rays, as

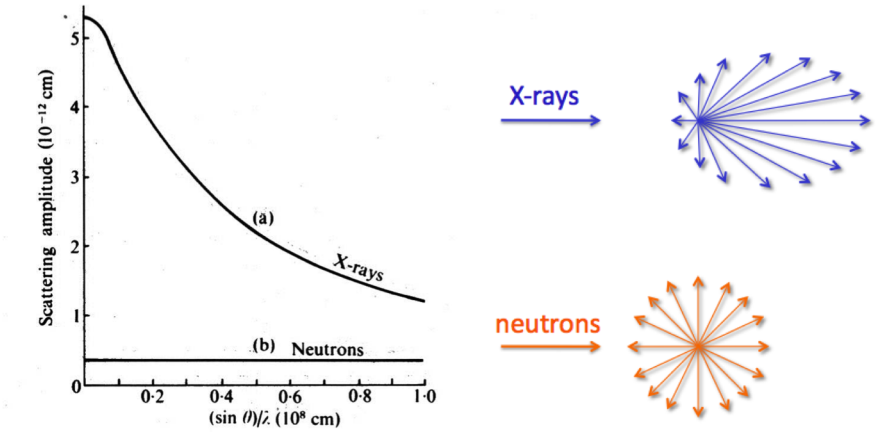

Figure 2.2: *Variation of scattering amplitude, f(q) with angle for a) X-rays and b) Neutrons*

the scattering from the electron cloud of a heavy element would overpower the signal from that of a light element.

Additionally, there are experimental benefits behind using neutrons as the radiating source, because neutrons are highly penetrating, with a penetration depth of cm→dm, enabling the beam to easily pass through the sample holder,containing e.g powder, or liquids, whereas x-rays are attenuated by matter and penetrate depths of μm-mm.

However, the intensity of the incoming neutron beam is lower than that of the x-ray beam,e.g for the same λ the incident flux (ϕ) of the x-rays is 10^{18} photons $s^{-1}cm^{-1}$, in comparison to neutrons which have an incident flux (ϕ) of 10^4 neutrons $s^{-1}cm^{-1}$. To account for the lower ϕ a sample of greater mass is required in neutron diffraction experiments and larger counting time.

2.6.1 Neutron Scattering

There are two types of neutron scattering events that can occur:

- **Coherent Scattering**: The resultant scattering is due to the diffraction effects of the nucleus of a static atom.
- **Incoherent Scattering**: The resultant scattering can be due to the diffuse movement effects, such as phonons, where the scattering is measured from an atom at t=0, and has moved relative to the initial scattering measured. In the case of coherent powder neutron diffraction, incoherent scattering just adds extra intensity to the diffraction pattern and can be treated as background noise in the data.

2.6.2 H and D Scattering Lengths

The neutron scattering length, b, measures the strength of how far the neutron is scattered by the nucleus. Each element has a different coherent and incoherent scattering length and cross section (we will consider only the coherent scattering length for the purpose of this investigation). The variation of b is uncorrelated with the elements in the periodic table as illustrated in Figure 2.3.

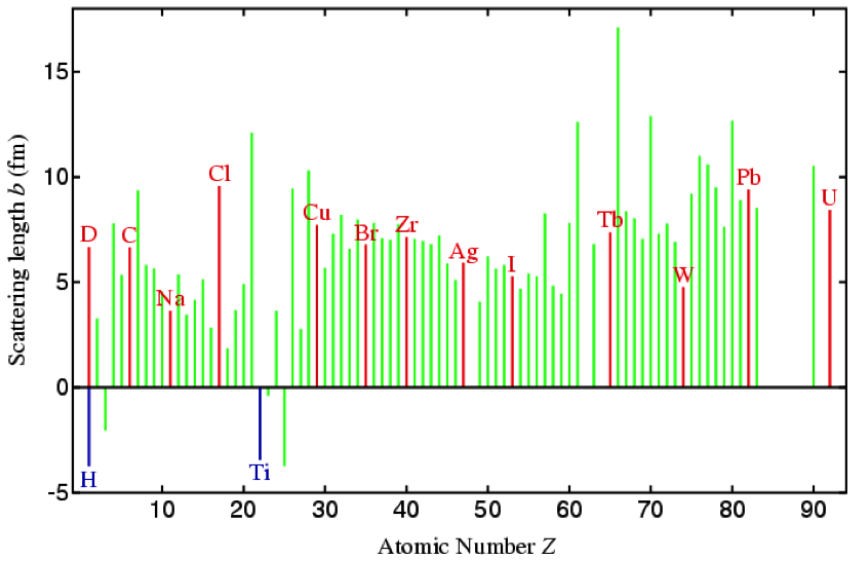

Figure 2.3: *Atomic Number of elements, z, against Scattering Length density, b (fm), [Cockcroft,J.K, http://pd.chem.ucl.ac.uk/pdnn/inst3/neutrons.htm]*

Deuterium, often described as 'heavy hydrogen' is an isotope of H which has 1 proton, whereas Deuterium has 1 proton and 1 neutron in the nucleus, hence the Greek name *deuteros* meaning second. It can be observed in Figure 2.3 that H has a negative coherent scattering length, H b_c = -3.74 fm. This negative sign implies a change of phase of the scattered wave in relation to the phase of the scattered wave of the positive scattering elements such as deuterium, ^2H, which has a scattering length of D b_c = +6.671 fm.

2.6.2.1 Isotopic Labelling

The difference in the coherent scattering lengths of D and H, can be utilised for **isotopic labelling** techniques, which currently play an important role in structural biology and polymer science research. This technique is adopted in this investigation by synthesising the NPs with selectively deuterated surfactants, with the aim of revealing information on the location and speciation of the surfactants on the NP surface. Neutron diffraction will enable the whole NP-surfactant system to be structurally probed using isotopic labelling, which is not possible using XRD analysis.

Chapter 3

Computational Modelling of the Nanoparticle-Surfactant System

The software program, PDFGui, can model NP and corresponding molecule PDFs separately through the refinement of lattice parameters, isotropic atomic displacement parameters, and atom positions for each model. A neutron diffraction investigation of an oxide NP (5 nm $BaTiO_3$) and the capping organic ligand benzyloxy by [Page et al., 2010], utilised this program to reveal the atomic correlations between the NP and ligand. The DIFFUSE package however has the capabilities to model the NP with the surfactant attached this enables the NP-ligand interaction to be probed. The example of this 3D modelling of fluoro-thiol capped gold is outlined in the flow diagram [Page et al., 2011] in the next section.

3.1 The Diffuse Scattering Und (and) Structure Simulation package

The Diffuse Scattering Und Structure Simulation, DIFFUSE, package, is an advanced PDF nanostructure modelling package designed by Reinhard Neder and Thomas Proffen , which consists of the following sub-programs: DISCUS, KUPLOT and DIFFEV, designed to run the different tasks, either independently or in combination. There is also the sub-program MIXSCAT, which can be used to extract differential PDFs from neutron and x-ray data. This is not however used in this investigation but its use will be considered for future analysis where required. This combined package has been used to simulate a wide range of structures, from perfect, disordered and infinite crystals, to glass, liquid and amorphous materials, and it has only recently been developed to enable the simulation of NPs.

3.2 'Nanoparticle Builder'

The flow chart in Figure 3.1 demonstrates the role each sub-program plays in building a NP using the experimental (observed) PDF data sets. In in this case the package was used to create a cuboctohedron of gold from neutron diffraction PDF data, and to identify surface sites, then decorate these sites with thiol ligands [Page et al., 2011]:

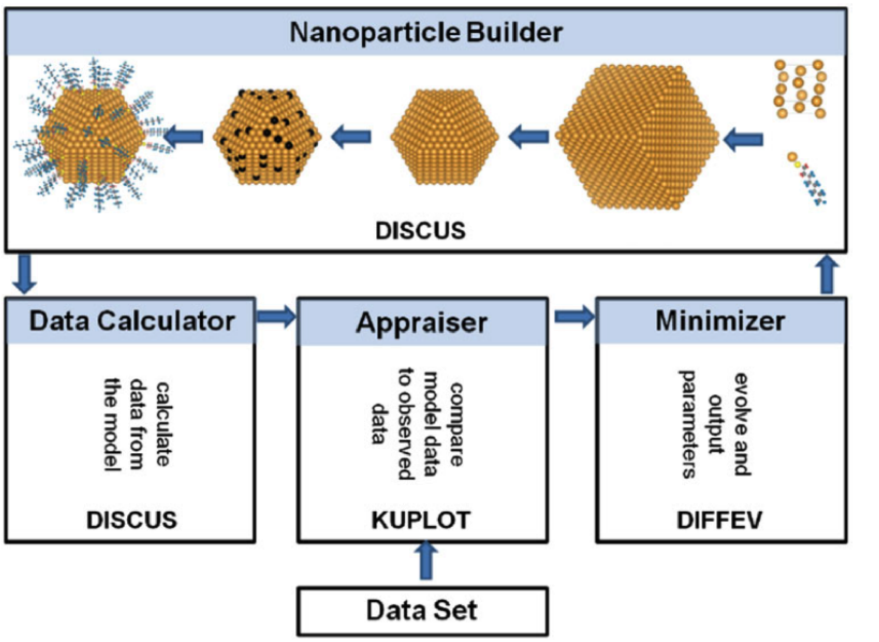

Figure 3.1: *DIFFUSE Package Flow chart demonstrating the Full Capabilities of the Software [Page et al., 2011]*

- DISCUS: Modelling package used to generate a model NP of arbitrary morphology (eg. core-shell, short-range order, disordered). A corresponding PDF data set can then be calculated based on the NP model created. This simulation of the NP system created can then be viewed in vacuum, using an interactive structure viewing program, JMOL. Further modelling using the DISCUS program can enable surface sites on the NP to be identified and ligands to be attached to these sites, with a defined ratio using a Monte Carlo simulation. This NP-surfactant model can then be refined again using DIFFEV in order to create the model that best fits the observed data set, creating a representative NP with ligands attached.

- KUPLOT: This data plotting package enables the PDF data sets to be displayed and allow for comparisons of observed and calculated data sets of the Models created in DISCUS. The r value for PDF peak identification can be also be obtained in the KUPLOT code

- DIFFEV: In order to determine the internal structure of the NP, with the closest representative (lowest R value) to the NP that was analysed, the calculated PDF data has to be refined with the observed PDF data. This is where the DIFFEV program comes into play. It is used for the refinement of the observed and calculated data sets over a prescribed range, using a differential evolutionary algorithm to generate the refined parameter values.

Generally, an assembly average of 30 individual NPs, is required to be compared and refined from the calculated data in order to obtain a model PDF that effectively represents the observed data.

In this investigation the DIFFUSE package will be used in a similar way to the method outlined above, in order to model FePt NPs from the data attained, and with the final aim being to model them with the capping ligands,acid and amine surfactants, attached.

Chapter 4

Materials and Methods

4.1 Materials

The reagents used in the synthesis of FePt NPs were all supplied from Sigma-Aldrich Ltd, UK:
$Fe(acac)_3$: Mw=353.17 g/mol, purity= 99.9 %, m.p= 210 °C
$Pt(acac)_2$: Mw = 393.39 g/mol, purity= 98 %, m.p= 249 °C
OA: Mw = 283.2 g/mol, purity= 99 %, = 0.895 g/cm3, b.p= 194 °C
OLA: Mw = 287.49 g/mol, purity= 70 %, = 0.813 g/cm3, b.p= 348 °C
HDA; Mw = 241.46 g/mol, purity= 98 %, = 0.7821 g/cm3, b.p= 330 °C

4.2 Solvent Degassing

The solvents that were added to the reaction were required to be degassed, and the following solvent degassing method was adopted for application to both dioctyl ether and ethanol.

The solvent was sealed in the Schlenk flask and was dropped in temperature, below its freezing point, by immersion into liquid $N_(2)$. When the solvent was completely frozen, the flask was put under vacuum for 2-3 minutes, with the flask still immersed. The flask was then closed and gently removed from the liquid $N_(2)$ and immersed in warm water (taking care not to jerk the flask) until the solvent had completely melted. This process is repeated (usually three times) and after the last cycle the flask was backfilled with an inert gas, in this case nitrogen. Degassed solvent in a sealed Schlenk flask can usually be kept for 1-2 days [Wipf, 2007].

4.3 Synthesis

The NPs synthesised for the XRD and Nimrod experiments were synthesised with a equiatomic composition, and of specific size, shape (round) and phase (fcc phase) and to exhibit a monodisperse distribution. Different synthesis methods were used to produce these NPs outlined below.

4.4 Sample 1 Synthesis Method

- Sample 1 was synthesised following the standard method as reported by [Rong et al., 2006]below using OA-H and OLA-H surfactants

The Fe $Fe(OEt)_3$ (0.5 mol) precursor was firstly added to the reaction flask in the glove box. The glove box is an enclosed inert N_2 environment required to prevent the oxygen in the air reducing the unstable Fe^{3+} precursor into the 2+ oxidation state. Once the flask was connected to the Schlenk set-up the Pt precursor $Pt(acac)_2$ (0.25 mol) was added along with the magnetic stirrer. The side arm was then sealed with a septum and the liquid solvents degassed dioctyl Ether, OA (5 mol) and OLA (1.5 mol) were added to the flask using a gas tight syringe that had been purged with N_2 before use. The temperature probe was then inserted into the reactant solution of the sealed flask. The water source to the condenser, and the magnetic stirring system (500 rpm) were turned on. The heating temperature was set at $287°C$ and the reaction was heated with the temperature increment profile and the colour change of the solution being noted. The reaction was refluxed for 30 minutes at $287°C$ before being removed from the heating mantle to cool to room temperature.

4.4.1 AM01 and AM06 Synthesis Method

NPs of a smaller size were required for the neutron diffraction experiments, in order to increase the sensitivity of the neutron diffraction statistics to the surfactants. Therefore a different synthesis process was carried out with the aim to produce smaller NPs as previously reported by [**?**]. This involved controlling the reflux time and temperature at which the reagents were added to the solution in order to have a tighter control over the nucleation and growth process.

- Sample AM01 was synthesised following the standard method outlined below using the OA-H and HDA-H surfactants
- Sample AM06 was synthesised followed the standard method outlined below using OA-H/D and HDA-H/D surfactants

The two metal precursors, $Fe(acac)_3$ and $Pt(acac)_2$ (0.5 mmol), were first added to the reaction flask and sealed (see Appendix for detailed apparatus). Degassed dioctyl ether (20 ml) was injected into the flask. The system was flushed with N_2 three times, the reaction flask was purged with N_2 for 30 min at room T, and the magnetic stirrer was turned on at the rate of 500 rpm. The contents of the flask wer heated up to 200°C and then left to reflux under a flow of N_2 for 30 minutes. The OA-H or OA-H/D (0.5 mmol) was then injected into the reaction flask and HDA-H or HDA-H/D (0.5 mmol) was added, whilst the temperature was kept at a constant 200°C (5°C above the b.p of OA). The reaction flask was sealed and the temperature was then raised to 295°C. The reaction was refluxed at this constant temperature, under the flow of N_2 for 4 hours. The heat source was then removed and the reaction mixture allowed to cool to room temperature.

4.4.2 Pure Product Sample Retrieval

Once the reaction flask had cooled, the final product was precipitated by addition of degassed ethanol (20 ml) and dispensed into a centrifuge tube using a glass pipette. The reaction flask was then washed with hexane (5 ml) to remove any remnant NP for collection.

4.4.3 Sample Redispersion

The resulting NP dispersion from the reaction flask was washed three times with polar ethanol and non-polar hexane, and centrifuged supernatant (waste) removed and the NPs were redispersed in non-polar-hexane.

4.4.4 Sample 1 Redispersion

10 mL of the pure product was dispensed into a centrifuge tube and centrifuged (at a standard step rate of 9 and T=20°C) at 3500 rpm for 10 minutes. The supernatant was discarded and 10 mL of the flocculate, ethanol was added. The sample was then vortexes for 1 minute and the centrifugation process was repeated twice. The final clean NP product was then redispersed in 10 mL of a nonpolar organic solvent, hexane.

4.4.5 Sample AM01 and AM02 Redispersion

The following redispersion procedure was tested against different centrifugation rates and times, and optimised to give NPs with monodisperse distribution. This centrifugation process is an important part of the NP dispersion, as too much ethanol can cause agglomeration, but not enough can prevent the NPs from being cleaned efficiently.

Ethanol (8 ml), was added to pure product (2 ml) in a centrifuge tube and centrifuged at 8500 rpm (higher rpm to separate small NPs) for 15 minutes. The supernatant was discarded, 5 ml of hexane was added; and the sample was vortexted for 1 minute to redisperse the NPs in solution. 5 ml of ethanol was then added. This centrifuging and redispersion of NPs was repeated twice at the reduced rate of 3500 rpm for 30 minutes each time. This allowed for the NPs to be cleaned effectively via this redispersion and separation process.

4.4.5

4.5 Transmission Electron Microscopy (TEM)

Transmission Electron Microscopy (TEM) is the main analytical tool that utilises high energy electron radiation to provide the information required to characterise the microstructure of a nanoscopic materials, such as NPs. The TEM microscope is the main analytical technique used to directly observe the size and distribution of the FePt NPs through the conventional method of bright field imaging.This *real space* image is created by inserting an objective aperture into the

back focal plane of the objective lens, the emerging electrons representing the spatial distribution in the form of phase contrast images.

4.6 ISIS: X-Ray Diffraction

Powder X-ray Diffraction (XRD) is an instrumental technique which utilises x-rays as the radiating source for the determination of the crystal structure of polycrystalline materials from the resultant diffraction pattern. In the case of laboratory sources, the characteristic x-rays are generated in a cathode ray tube where high energy electrons from a filament are directed at a specific anode target such as Co or Ag, depending on the degree of resolution required. The anode target, has a mean shorter characteristic K^{α} wavelength λ, 0.5609 Å(Ag), than that of the standard laboratory Co target. The x-rays are then filtered using a monochromater, collimated and then directed at the rotating sample.The diffractometer scans the sample over a range of 2θ angles,in order to collect the scattering from all random orientations of the powder sample. The ISIS diffractometer has a maximum scattering angle near 156 °, giving a Q_{max} of 21.9 $\mathring{A}^{-1}$ [Soper and Barney, 2011], these measurements are usually taken to obtain complementary x-ray data for further neutron PDF analysis.

4.7 ISIS: Neutron Diffraction

4.7.1 Neutron Source

There are two main neutron sources that are used to produce neutrons; **spallation sources** which can either be time of flight spallation sources (ISIS with 200kW) or continuous spallation sources (SINQ at PSI,Paul Scherrer Institute; and **Fission-Nuclear reactor sources** (ILL, Institute Laue-Langevin). The ISIS facility at the Rutherford Appleton Laboratory, Oxfordshire houses the UK's only neutron facility. The neutron source firstly requires a supply of heavy charged H^- source. The H^- ions are then accelerated along a linear accelerator (linac) and directed through a stripper, which strips the H^- electrons creating protons,H^+. These protons are then accelerated further and enter the main synchrotron proton storage ring, utilising a magnetic field (B-field) to bend the beam, and an electric field (E-field) to accelerate the beam, and a combination of the E- and B -fields to focus the beam.

The 160 kW proton beam is then directed, to a heavy metal target tantalum (Ta). The collision of the proton beam into the nucleus of the Ta atoms results in **spallation**, which is the disintegration of the nucleus, causing the emission of $\sim$ 40 neutrons/proton. The neutrons are then directed into two different moderators; Target Station 1 (TS-1) with solid tungsten moderator or to Target Station 2 (TS-2) with a water cooled coupled solid CH_4 and decoupled poisoned solid CH_4 moderator. The moderator is used (in the case of spallation sources) to slow down the high energy neutrons before entering the diffractometer.

The basic concept of a time of flight pulsed-source is that neutrons travel in 'packets' with a specific time interval between each packet e.g the time interval is $\sim$ 20 ms for ISIS-TS1 and $\sim$ 100 ms for ISIS-TS2) this interval tunes the λ of the neutrons e.g as the time interval between

the time pulse,t $\downarrow$, E $\uparrow \Longrightarrow \lambda \downarrow$. The bunches of neutrons are then channelled through guides and accelerated at different λ into 20 different beamlines.This time of flight spallation source used by ISIS will give better resolution at high angles, allowing for low d-spacing analysis, and higher neutron flux allowing for faster collection time, in comparison to reactor sources.

4.7.2 ISIS: Near Intermediate Range Order Beamline

The Near Intermediate Range Order beamline, Nimrod consists of a wide range of detectors with continuous Q range from 0.01Å^{-1} to 50Å^{-1}, that bridges the gap between small angle and wide-angle neutron scattering [Bowron et al., 2010]. It is intended to take advantage of this, for effective analysis of the whole NP system, from the surrounding atom-atom surfactant to the shortest internal correlations. The ISIS instrument is designed specifically to minimise the incoherent scattering associated with H, enabling systems with the presence of hydrocarbons (such as surfactants) to be easily interpreted. The use of a forward-scattering geometry (in Nimrods case only considering scattering angles up to 40 °) and relatively high-energy neutrons assists in this process as they reduce the degree of inelastic events measured.

Chapter 5

Experimental

5.1 Bright Field Transmission Electron Microscopy

The technique of Transmission Electron Microscopy (TEM) in bright field mode was used in this investigation on a JEOL JEM-1200 EX electron microscope, that has an accelerating voltage of 120 kV.

5.1.1 TEM sample Preparation

1 μl of the clean NP solution, dispersed in 1 ml of hexane, was dispensed into an epindorph tube containing 1.4 μl of hexane using an organic dispenser pipette a 0.5 μl drop of the sample was dropped onto a carbon-coated TEM grid and held until the hexane evaporates. It is important that the solution is properly dried to ensure no solution is trapped in the grid.

5.2 Sampel Preparation and Data Acquisition

The first stage of this NP PDF analysis process was carried out collaboratively with Dr. David Keen, utilising a monochromatic laboratory $Ag^{+}K_{alpha}$ x-ray diffractometer, based at ISIS. The diffraction pattern measurements were taken from the dried FePt NP sample in a quartz capillary sample holder, and were run for a period of 74 hours.

5.2.1 XRD Sample Preparation

The clean evaporated NP solution was dispensed into a 1 mm quartz capillary and dried carefully by manual rotation of the sample. The sample was dried 1 mm away from the end of the capillary and covered the surface of the capillary over the lower 1 cm region of the capillary. The results obtained were found to be most successful when the sample was dispersed evenly around the inside of the capillary walls.

5.2.2 Neutron Sample Preparation

The NPs did not remain suspended in the D-hexane solution long enough for the runs that would be required to attain good statistics. The NPs were therefore evaporated from the hexane solution drop by drop into the 5cm x 5cm cut out of the Titanium Zirconium (TiZr) sample holder, with a volume of 1 cm^3. The TiZr material, has very low negative scattering and is ideal as a sample holder in neutron scattering experiments. The dried NP sample was then sealed into the can using the flat plate lid.

5.2.3 Neutron Diffraction Data Acquisition

Time-of-flight neutron diffraction experiments were carried out on the beamline, Nimrod at ISIS. The wavelength was set at a start at 0.15 Åbecause of the presence of Pt the NPs. This was to avoid any resonances associated with the metal, but results in the maximum Q-range in the resultant PDFs were reduced from 50 to 20 $\mathring{A}^{-1}$. The exposure time required to obtain a high enough scattering intensity data with counting statistics suitable for PDF analysis was 9 hours. However, the Sample AM01 was only run for for 7 hours and Sample AM06 was only run for 4 hours due to an instrumental problem that incurred preventing a longer run time.

5.3 XRD and Neutron Diffraction Pattern Normalisation and PDF

The powder XRD data and neutron diffraction data acquired from the samples was normalised and processed computationally using an in-house software program, GudrunX and GudrunN, designed by Dr. David Keen [[A.K., 2011]]. Data processing of the normalised x-ray and neutron diffraction data from Sample 1 and Sample AM01 & AM06 was carried out, using the GudRunN and GudRunX program, to give the corresponding real space PDF. The results of the resultant PDFs were plotted again using KUPLOT.

Chapter 6

ISIS XRD-PDF Results and Analysis

The XRD-PDF analysis of Sample 1, utilising the Ag $^{+}K_{alpha}$ laboratory source x-ray diffractometer at ISIS, was carried out in order to validate the sensitivity of the PDF technique to the sample being analysed. This was done with the intention of confirming whether or not, the PDF would be sensitive to the FePt inter-atomic bonding distances and NP size. This test procedure is routinely carried out at ISIS before going on to carry out more accurate (but expensive) neutron diffraction measurements of greater resolution.

6.1 TEM Images of Sample 1

Sample 1 was synthesised using the standard Pt precursor, $Pt(acac)_2$, the Fe precursor, $Fe(OEt)_3$, with a 2:1 ratio of Fe:Pt and a 3:1 ratio of OA:OLA surfactant (see Section 4.4 for detailed method). The lighter contrast regions present on the micrographs are expected to be due to

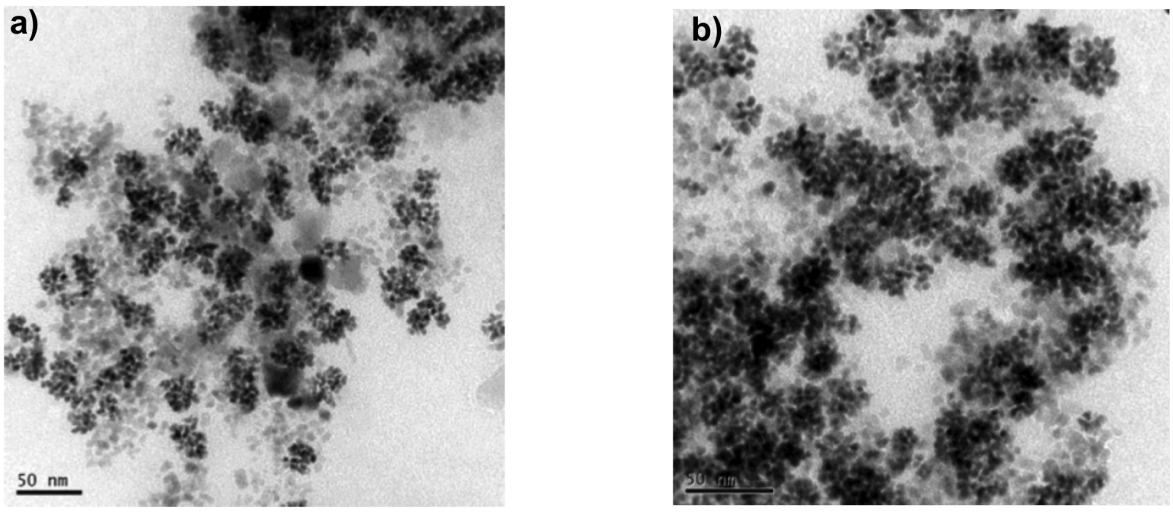

Figure 6.1: *TEM Micrographs of Sample 1, clusters of FePt NPs with an average diameter of 4 nm (40 Å) a) Mag. x30 kV and b) x40 kV with 50 nm scale-bar inset*

excess Fe precursor that has not reacted during the synthesis. This unreacted material could also explain the clustering of the NPs, as the excess Fe, surrounded by OA surfactant, will result in the lack of OA on the surface of the formed FePt NP.

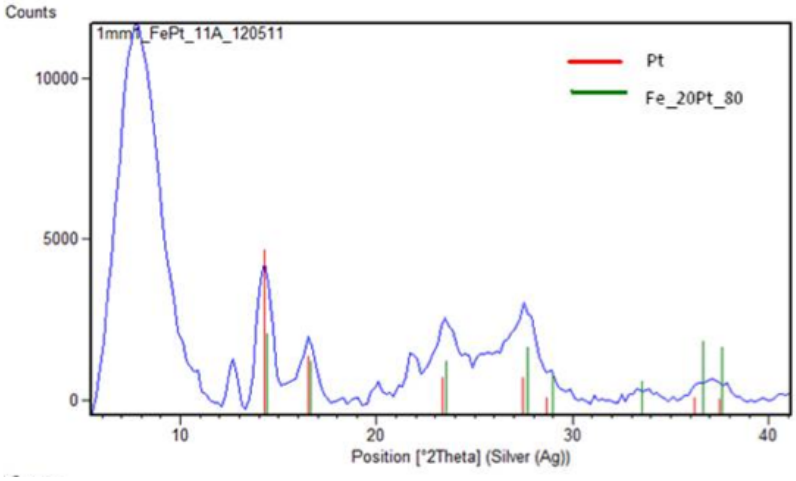

Figure 6.2: *Diffractogram of Sample 1, using an Ag diffractometer, confirms the presence of* $Fe_{20}Pt_{80}$ *(Ref:00- 029-0717) and the closeness of the parameters to Pt (Ref:00-001-1194)*

This theory coincides with the composition of the NP $Fe_{20}Pt_{80}$ obtained from the indexed XRD pattern in Figure6.2. Furthermore, the first three indexed Bragg peaks; (111), (002), and (202), correspond to the signature peaks of the fcc planes from FePt NPs. Additional peaks are due to the presence of impurities within the sample. These impurities present are an anomaly and could be due to a leak in the taps during synthesis resulting in the introduction of O_2 at a vital stage of the NP formation process.

6.1.1 XRD Pair Distribution Function of Sample 1

The PDF sine Fourier Transform equation, outlined in Chapter 2, was applied to the normalised diffraction data obtained from Sample 1, converting it from reciprocal space into a real space PDF, Figure 6.3.

Analysis of the peaks of the atomic PDF in Figure 6.3 allowed for determination of the FePt NP NNs. The intra-atomic distances of the 1st, 2nd and 3rd NNs were identified from the PDF as Fe-Fe 2.49 (2.566)Å, Fe-Pt 3.720(3.794)Å, Pt-Pt 4.57589 (4.570)Å, respectively. These bond distances were acceptably close to the theoretical calculated values in brackets obtained from the model FePt PDF created of a standard fcc FePt NP in section 8.1. The shortest, most dominant bond, Fe-Fe, is present due to the fcc structure. Also, due to the dominance of the metals in x-ray scattering, the initial peaks represent the shortest internal correlations expected for this chemically disordered fcc metal alloy. It can be observed that the peaks diminish at an average real space bond distance,r, of an average r of 4 nm (40Å), corresponding to the largest possible bond distance within the NP. This 'cut-off' indicated by the dashed line in Figure 6.3 represents the quantitative average diameter of the NP.

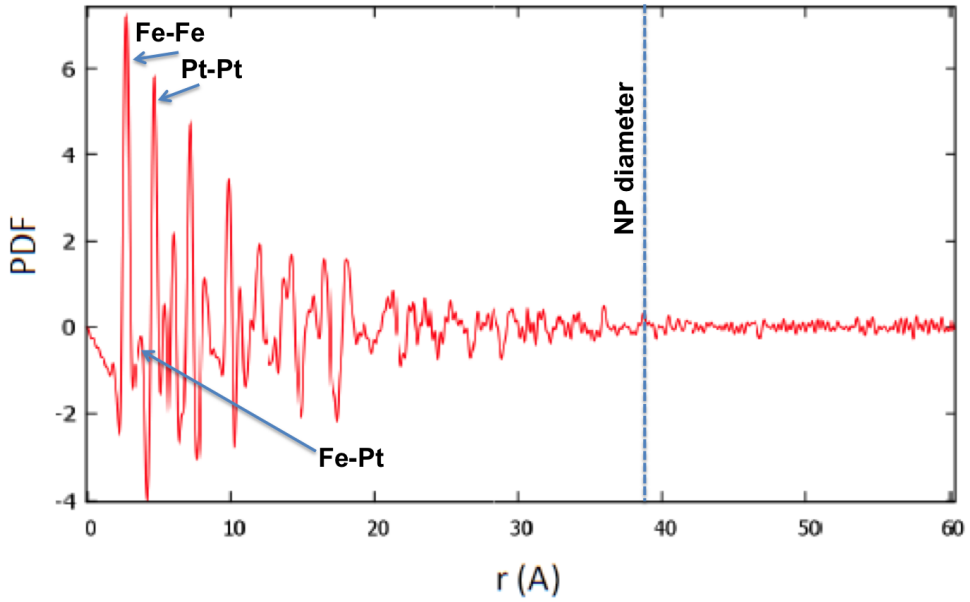

Figure 6.3: *XRD-PDF of sample 1 with asigned peaks representative of the FePt nearest neighbour distances within the NP, and dashed line indicating the average diameter of 40 Å*

6.1.2 ISIS XRD-PDF Conclusion

The XRD-PDF results acquired from ISIS Ag $^{+}K_{alpha}$ laboratory source x-ray diffractometer validate the sensitivity of the PDF technique. Quantitative analysis of the PDF revealed interatomic bond lengths of fcc FePt which correlated well the theoretical bond length values. Also, the PDF yields a NP size of 40 Å(4 nm), in good agreement with the size obtained from the TEM images. The results obtained from the XRD-PDF confirms that the PDF technique applied to powder diffraction patterns of FePt NPs is effective and allows for the continuation of the application of this technique to diffraction patterns obtained from neutron diffraction measurements.

Chapter 7

NPDF Results and Analysis

Samples AM01 and AM06 were synthesised for Nimrod neutron diffraction measurements using the standard Pt precursor $Pt(acac)_2$ and the Fe precursor, $Fe(acac)_3$, with a 1:1 ratio of Fe:Pt and 1:1 ratio of OA:HDA surfactant. AM01 and AM06 were synthesised with hydrogenated surfactants (OA-H and HDA-H) and par-deuterated surfactants (OA-H/D and HDA-H/D), respectively (see Section 4.4.1 for detailed synthesis method).

7.1 TEM Images of Sample AM01

The TEM micrographs of Sample AM01 in Figure 7.1a) and Figure 7.1b), show that the sample consists of spheres of monodisperse NPs of average diameter 20 Å(2 nm).

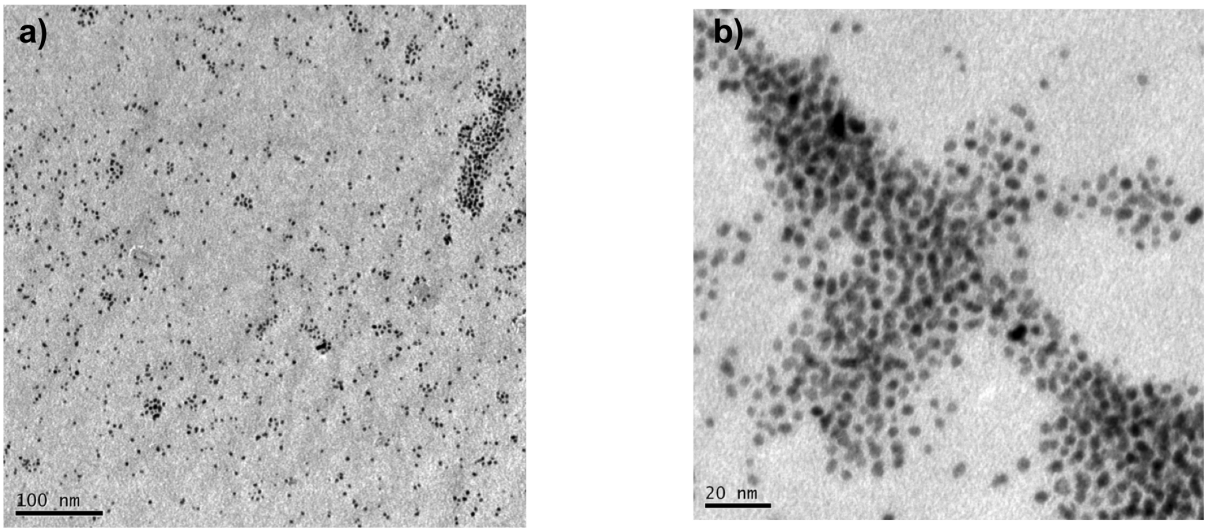

Figure 7.1: *TEM Micrographs of Sample AM01: 20 Å(2 nm) spheres of FePt NPs with a monodisperse distribution taken with a)Mag. x20 kV with 100nm scale-bar inset and b) Mag. x75 kV with 20nm scale-bar inset*

The lack of any impact on the observed NPs proves that using the amine surfactant HDA as a substitute for OLA did not affect the NPs shape and distribution in comparison to the results

attained from the same synthesis method using OLA. *Note the results from the par-deuterated samples were not imaged due to the whole sample being used in the neutron diffraction analysis, micrographs of the recovered sample will however be be taken*

7.2 Neutron Powder Diffraction Pattern Analysis of Sample AM01 and AM06

The normalised diffraction patterns were acquired from the neutron diffraction measurements of the two samples; AM01 with hydrogenated surfactant illustrated, in Figure 7.2 (a), and AM06 with par-deuterated surfactant, illustrated in Figure 7.2 (b). The following fcc planes (111), (200), (220), (311) and (333) are indexed on both diffraction patterns. These signature peaks confirm the presence of the fcc FePt NPs.

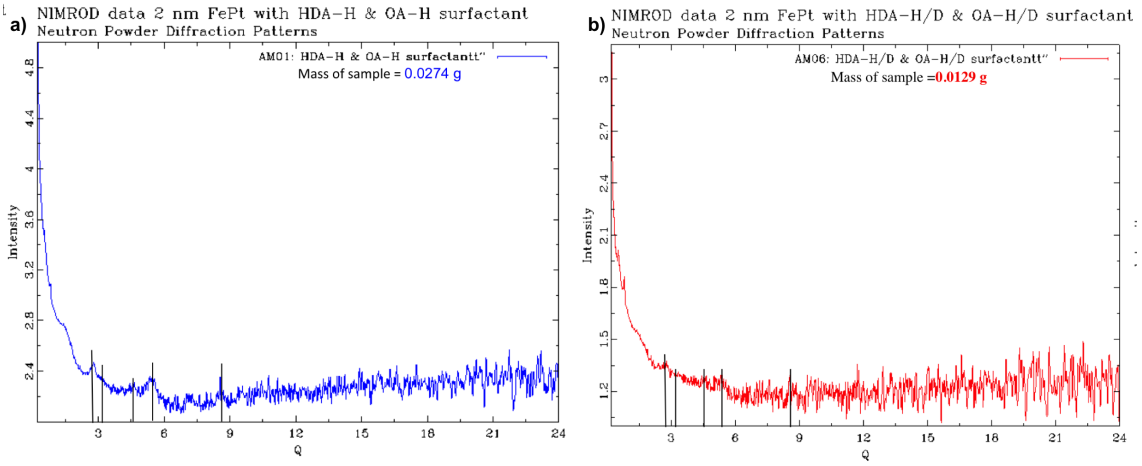

Figure 7.2: *Neutron Diffraction Patterns acquired from samples AM01 with hydrogenated surfactants(blue line) and AM06 with par-deuterated surfactant (red line) with the signature fcc FePt NP peaks indexed*

The mass of sample AM01 (0.0274 g), was 52 % (0.0145 g) less than the mass of sample AM06 (0.0129 g), this lower % mass explains the weaker signal acquired from sample AM06. Also, notably the run time for sample AM06 was less than that of AM01 due to technical problems at the ISIS facility resulting in the loss of beam. This factor also contributed towards the lower statistics acquired from sample AM01.

7.2.1 Comparison of AM01 and AM06 Diffraction Patterns at Low Q

The low Q region of the neutron diffraction patterns obtained from samples AM01 and AM06 were over-laid for comparison and there is an observable difference between sample AM01 (hydrogenated) and AM01 (par-deuterated).

Firstly, the slope of AM01 is of higher intensity compared to that of sample AM06. This steep rise in intensity, is suggested to be due to the presence of H background as the effect of elasticity is being present at low Q [A.K., 2009]. Also there are additional peaks in sample

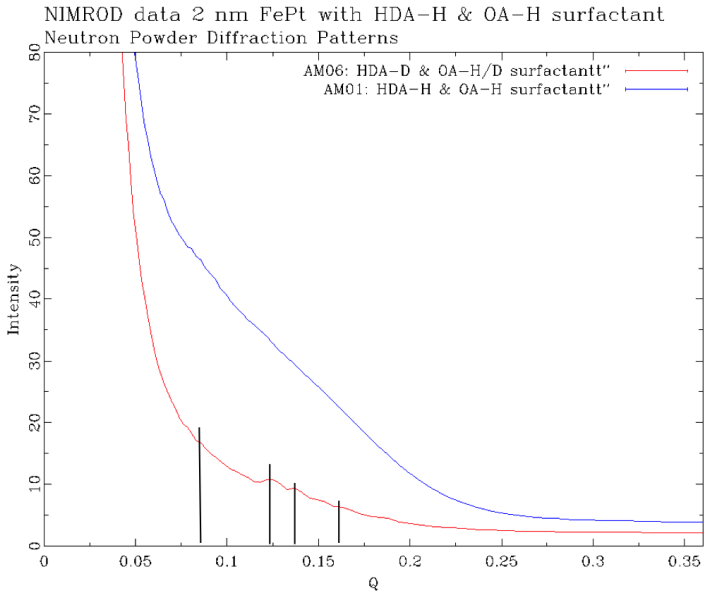

Figure 7.3: *Low Q comparison of Neutron Diffraction Patterns acquired from samples AM01 and AM06, with additional peaks from the deuterated sample AM06 indexed*

AM06, which are not apparent in sample AM01. These additional peaks from the par-deuterated sample AM06 are indexed and it is hypothesised that these peaks correspond to a crystallised surfactant either OA or HDA. Future investigations into the structure of these crystals and their corresponding diffraction patterns is required in order to confirm this hypothesis.

7.2.2 Nimrod Neutron PDF Analysis of AMO1 and AM06

The two PDFs obtained from samples AM01 and AM06 were compared in Fig 7.4. The distinct baseline of AM01 is also expected to be due to added intensity arising from hydrogen background of the H-surfactants. The PDFs contain information about the whole NP surfactant system where the dashed lines indicated in Figure 7.4 contain the following structural information:

- The point below the NN atom-atom distance of the FePt NP, is indicated by the dashed line; any prominent peaks before this point are due to the intramolecular bonding in the surfactant and the bonding between the surfactant and NP surface (as detailed in Figure 7.5 and Figure 7.6)
- The peaks beyond the first dashed line correspond to the intramolecular bonding of the NP. Also, intermolecular distances within the NP and surfactant will be present in this region until the diameter of the NP is reached at 20 Å
- Before the final dashed line the additional peaks correspond to the longest surfactant-surfactant atomistic distances within the NP-surfactant structure

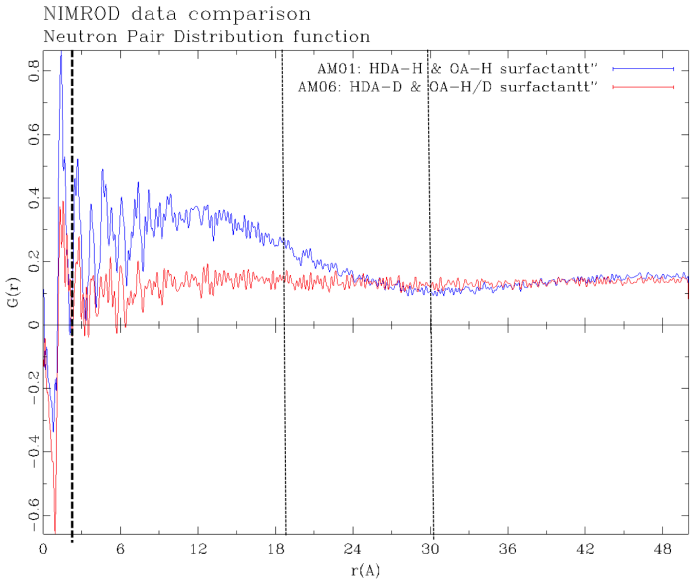

Figure 7.4: *Low r region of AM01 PDF with specific peaks labelled with corresponding bonds, table inset with theoretical and experimental bond lengths*

7.3 Surfactant Bond Lengths

Close inspection of the low r region of the PDF in Figure 7.5 and Figure 7.6 shows additional peaks that are expected to be due to immediate intramolecular bonding in the surfactant and between the NP and the surfactant:

7.3.1 Low r Region Analysis of PDF from Sample AM01

Expected Bond lengths were assigned to peaks indicated in Figure 7.5. The r-values from the

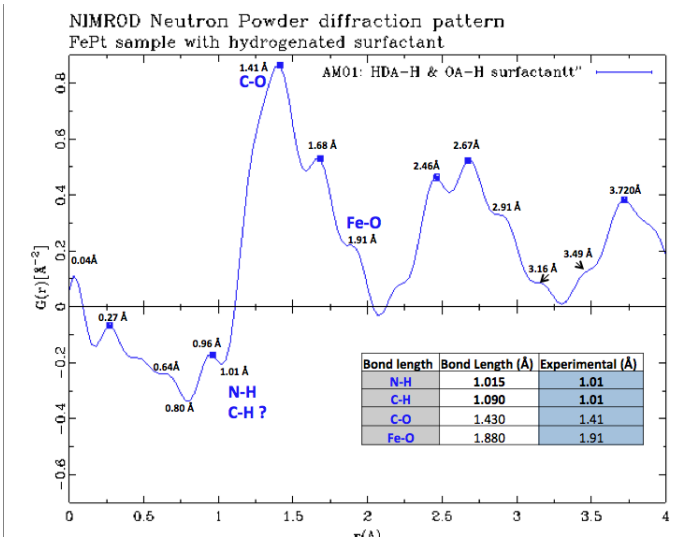

Figure 7.5: *Low r region of PDF from sample AM01, with assigned bonds, table inset with theoretical and experimental bond lengths bold values represent that there are other possible matches*

peaks, correspond well with the theoretical bond length values [Frank H. Allen et al] of C-O, and Fe-O, as detailed in the table inset. The negative peak at r = 1.01Åis expected to be due to the C-H, N-H or C-H bonds, as outlined in the table in bold, with the closest match being N-H. The C-O bond could be due to the carbonyl group of the OA COO^- which is bonded to the Fe on the surface, or within the surface of the NP. However, as this peak is the most prominent this is unlikely, and it could be the case that the peak from the C-C (theoretical value = 1.32 Å) and C=C (theoretical value of 1.56 Å) has merged, as the carbon backbone of the surfactant is the most prominent feature. The Fe-O is expected to be due to the carbonyl group of the OA COO^- bonding to the Fe on the surface, or within the surface of the NP.

7.3.2 Low r region Analysis of PDF from Sample AM06

Expected bond lengths were assigned to peaks indicated in Fig 7.6, these r-values correspond well with the theoretical bond length values of C=C, C-C, Fe-O and Pt-N, as detailed in the table inset [Frank H. Allen et al]. The C-C carbon peaks are most prominent and is expected to be due to the carbon backbone of the surfactant. The C=C is expected to be due to the double

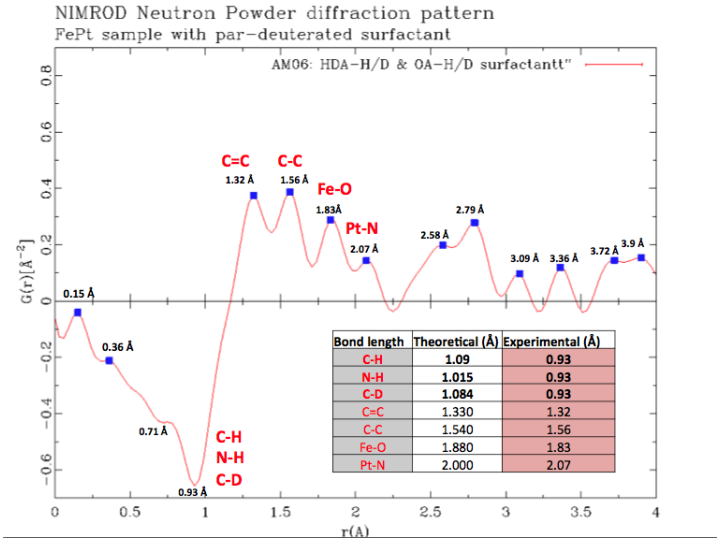

Figure 7.6: *Low r region of PDF from sample AM06, with assigned bonds, table inset with theoretical and experimental bond lengths bold values represent that there are other possible matches*

bond in the OA backbone. The Fe-O is expected to be due to the carbonyl group of the OA COO^- bonding to the Fe on the surface, or within the surface of the NP, and the Pt-N bond is expected to be due to the NH_2 group of the HDA bonding to the Pt of the NP. The negative peak at r = 0.93 Åis difficult to allocate a specific bond to. the potential matches of N-H or C-H are outlined in the table in bold, with the closest match being N-H. The C-D bond could be ruled out, as the negative peak is expected to be due to the negative scattering length of H. This scattering, therefore, could be from the combination of the C-H signal from the surfactant backbone and N-H from the amine of HDA. However, this peak is large in comparison to the small peak at r= 1.01 Å, that is also assigned to the bond length of C-H or N-H. It is expected that the reverse would be the case due sample AM01 consisting of fully hydrogenated surfactant and being of a greater mass than sample AM06.

Overall, more assigned bonds were obtained from the peaks of the PDF in sample AM06 than from those of AM01. It is proposed that the peaks of these bonds are more obviously apparent, and this could be contributed to the use of the par-deuterated surfactant.

7.4 FePt Nanoparticle Nearest Neighbour Bond Lengths

Close inspection of the central r-range, 2-6 Å, of the PDF in Figure 7.7 and Figure 7.8 enabled the 1st, 2nd and 3rd nearest neighbour bonds in the FePt NP to be asigned to the peaks with the closest match to those obtained from the model PDF in section 8.1.

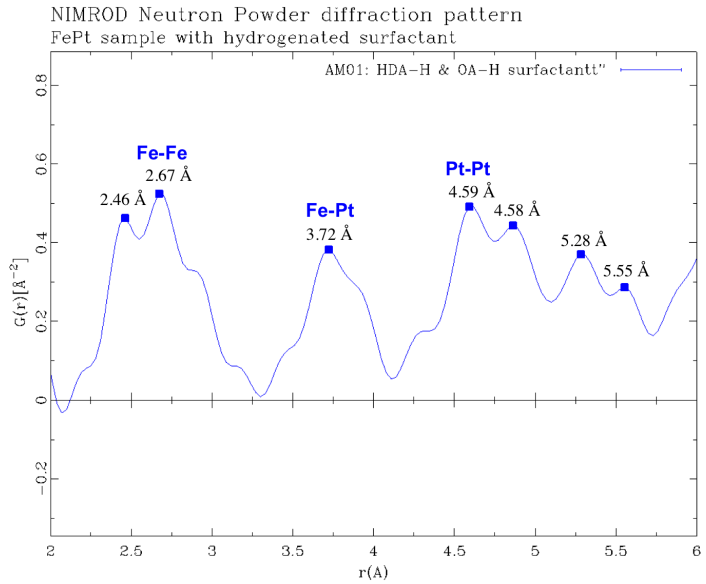

Figure 7.7: *Central r range of PDF from sample AM01 from 2-6Å, with specific peaks assigned to NN bonds of FePt*

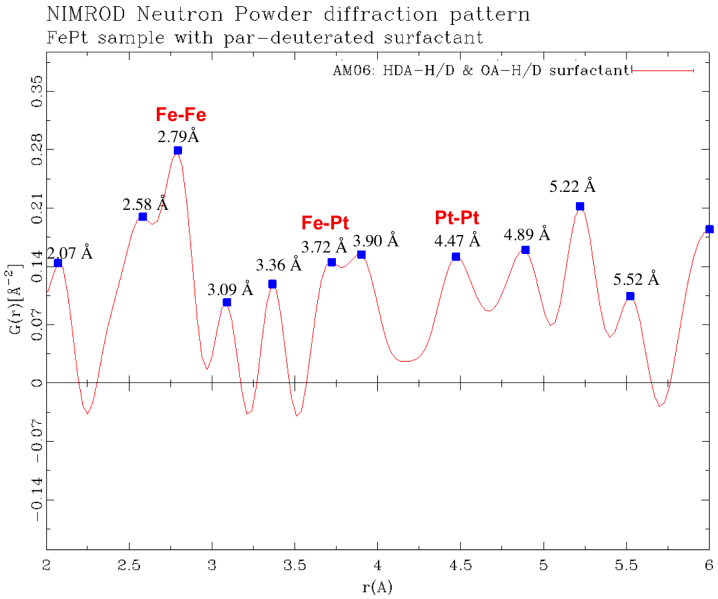

Figure 7.8: *Central r range of AM06 PDF from 2-6Å, with specific peaks assigned to NN bonds of FePt*

The NN peaks in sample AM01 and AM06 were assigned to the Fe-Fe, Fe-Pt and Pt-Pt bonds, the r values of these bonds are in good agreement with those obtained from the model. The peaks asigned to AM06 are again more reliable than those from sample AM01.

7.5 NPDF Conclusion

The data obtained from these first neutron diffraction measurements at Nimrod, had lower than planned statistics, due to loss of beam, but still the unique 111 reflections of the FePt fcc phase were easily identified, thus proving the high sensitivity of the diffraction pattern analysis of these NP systems, even at low NP concentrations. The differences in the PDFs identified for sample AM01 of FePt NPs with hydrogenated surfactant, and sample AM06 with par-deuterated surfactant, illustrated the pronounced benefit of probing the structure of the surfactant using isotopic substitutions. Also, in this resultant PDF of the NP-surfactant system, structural information about the surfactant was identifiable before the first nearest neighbour peak of the NP.

Also, the bonding information obtained from the PDF peaks proves the bonding hypothesis [Sun, 2006],[Suda et al., 2007], that the Fe atoms on the surface of the NP are specifically associated with the carbonyl group of the surfactant through Fe-O bonds, while the Pt atoms are associated with the amine group of the other surfactant via Pt-NH_2 bonds.

Further information that could be discovered about the ligand from the PDF calculation could be obtained by dividing the PDF by the average squared scattering length of the ligand, as this changes with ligand contribution. The requirement for improvements and alterations to the experiment will be applied in the next round of beamtime as discussed in Chapter 9.1.

Chapter 8

3D Nanoparticle Modelling

The PDFs of FePt NPs were modelled with the same Q factor and radiation wavelength as the experimental diffraction data. In order to model the FePt fcc NP, the unit cell was obtained from the Inorgranic Crystal Structure Database (ICSD) and the parameters were input into a macros file.

8.1 FePt Nanoparticle Nearest Neighbour Model

A 3D model of a randomly distributed fcc FePt NP was created and the nearest neighbour bond distances were defined as illustrated in 8.1.

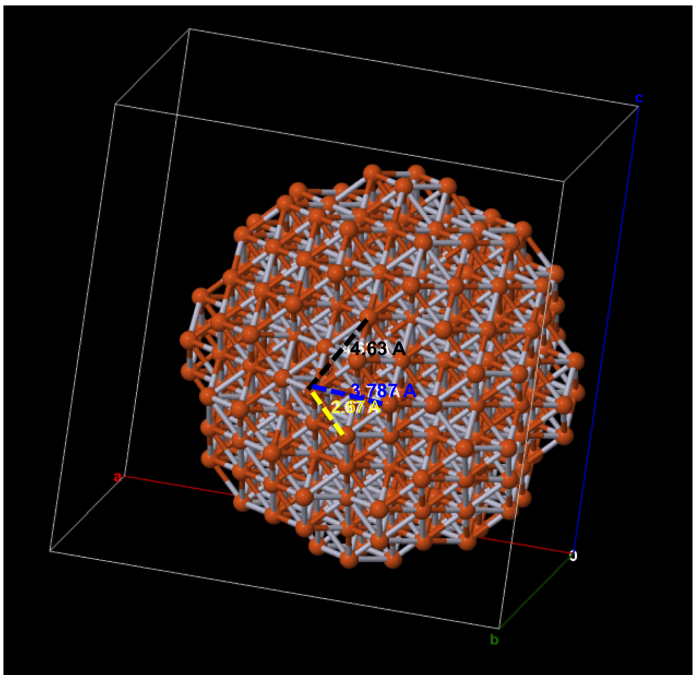

Figure 8.1: *3D model of 20Åfcc FePt NP with the 1st nearest neighbour bond (yellow dashed line) being from Fe-Fe, 2nd nearest neighbour bonds (blue dashed line) being from Fe-Pt and the 3rd nearest neighbour bonds being from Pt-Pt (black dashed line)*

8.2 Model of FePt Nanoparticle Size Effects on PDF

3D models of FePt NPs of different size with randomly ordered structures were modelled and their corresponding PDFs obtained. The PDFs of the FePt NPs modelled with a diameter of 20Åin Figure 8.2(a) and 40Åin Figure 8.2(b) demonstrate the size effects of the NP on the PDF.

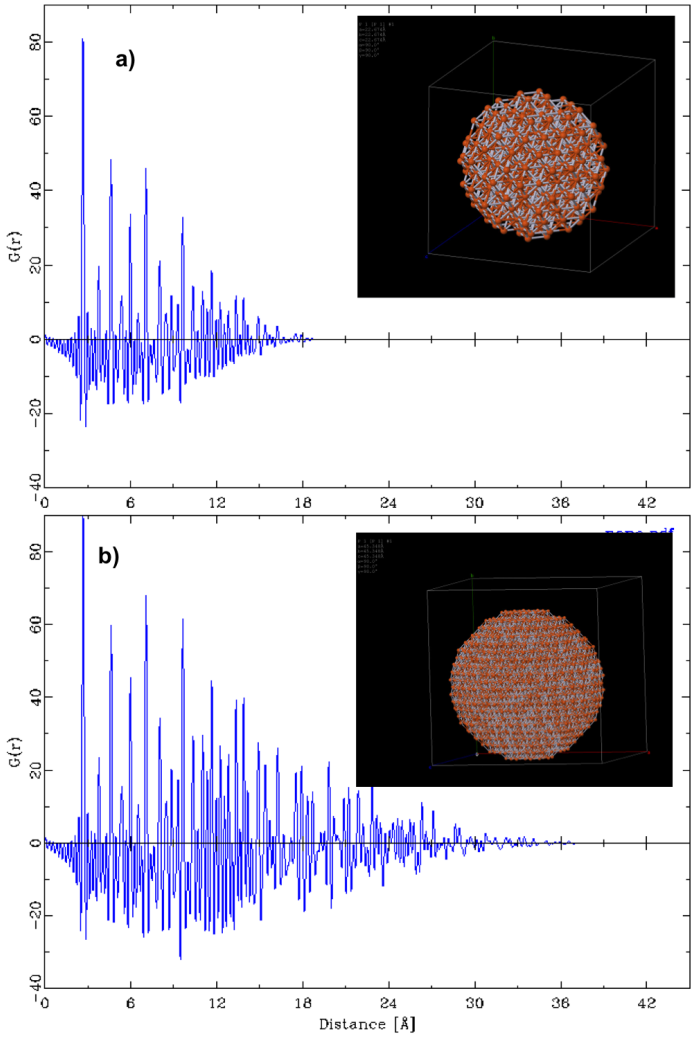

Figure 8.2: *Model FePt NP with corresponding PDF a) 20ÅFe50Pt50, 642 atoms b)40ÅFe50Pt50, 982 atoms*

The diameter is represented by the point at which the largest atom to atom distance has been reached and is clearly demonstrated by the termination ripples in the PDFs at 20Åand 40Å. This result confirms that the calculated PDFs obtained from the model FePt NPs, created using DISCUS, behave as expected for a NP system.

8.3 Core-shell Model

8.3.1 FePt@Pt

A 3D core-shell model of an 18ÅFePt@Pt NP with random distribution was created with a core of randomly correlated Fe and Pt atoms and a 2Åthick shell of Pt atoms. The core-shell model of the NP with the corresponding calculated PDF of this model is illustrated in Figure 8.3.

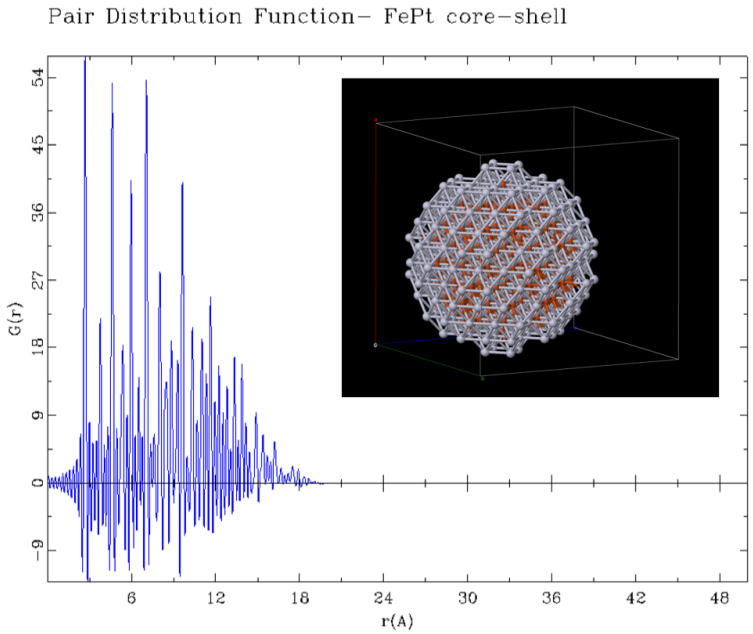

Figure 8.3: *Model of Core-shell FePt@Pt with corresponding calculated PDF(643 atoms, Fe abundance= 141 Pt abundance= 501)*

The slightly higher baseline in the core-shell PDF model demonstrates that changing the internal structure of the NP model has an effect on the corresponding calculated PDF.

8.4 Progress in Ligand Attachment

8.4.1 Identification of Surface Sites

The first step in the process of modelling the FePt NP with ligands is to define a percentage of surface sites in which the ligands will be attached to. This is done by substituting a surface atom with a 'dummy' atom, of similar Z, in order to separate the surface sites out from the rest. The dummy atom is inserted firstly at the origin and the loop defined to find all atoms a distance greater than a radius of 7.7 Å, (so they will be placed at 1.3 Åin the NP surface) and the dummy atom is inserted if there are no neighbouring dummy atoms within the defined ratio. This user defined ratio of Fe or Pt atoms (in this case Pt) at the surface of the NP is specified and substituted with dummy atoms,for ligand attachment.

These steps were carried out on a 20 Ådisordered FePt NP to identify different numbers of surface sites on the FePt surface where in Figure 8.4 (a) Au dummy surface site atoms of a

ratio 0.5 within a separation distance of 5Åwas defined and in Figure 8.4 (b) Au dummy surface site atoms of a ratio 0.5 within a separation distance of 3.72 Åwas defined.

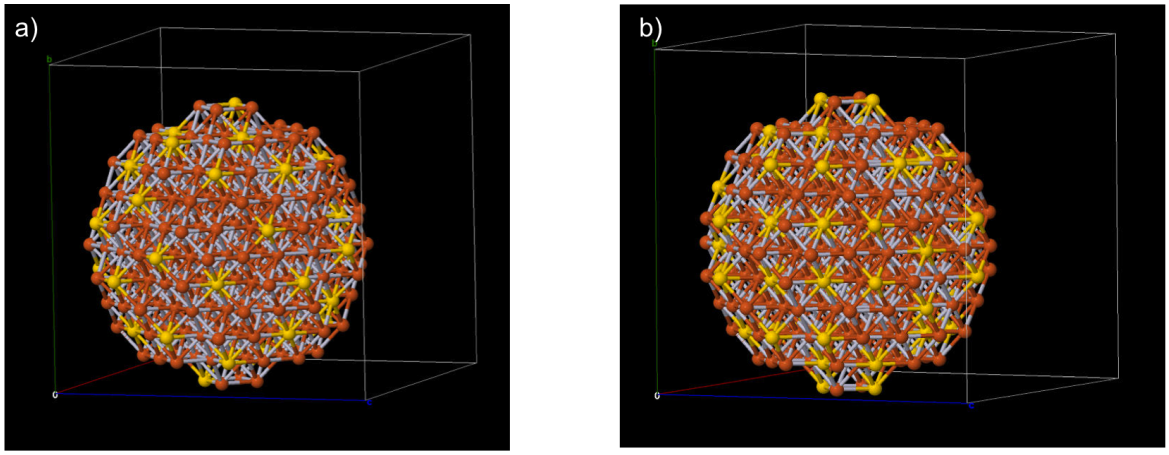

Figure 8.4: *3D model of 20 ÅFePt NP with 643 atoms and surface sites defined by the dummy atoms Au (yellow atoms), with a) an Au atom ratio of 0.9 within distance of 4 ÅFe abundance= 283 Pt abundance= 283 Au abundance = 76) and b) an Au atom ratio of 0.5 within distance of 3.72 Å, Fe abundance= 270 Pt abundance = 270 and Au abundance =102*

The models of different surface sites can be used to determine the number of potential surface ligands e.g 76 HDA surfactant molecules would be attached in Figure 8.4 (a) and 102 HDA surfactant molecules would be attached in Figure 8.4 (b). The program to be adapted further in order to combine it with the ability to define a ratio of Fe surface sites for the ligand attachment of the OA surfactant aswell.

8.4.1.1 Outline of Ligand Attachment Procedure

The ligands' structure, i.e the structure of the surfactants OA and HDA, is firstly required to be obtained and the ligands successfully modelled. On completing this, it is required that ligands are orientated parallel to each other and the carbon backbone of the ligand is to be orientated to the normal of the surface (in the case of Au in the [100] direction) to prevent the program from automatically aligning the ligands in one direction on the NP surface causing the ligands on one side to point into the NP. Further work on the development of the ligand attachment code is required to orientate the ligands effectively on the surface. Also, modelling an FePt alloy with the corresponding OA and HDA surfactants is a new approach and at the time of print no other investigations have used the DISCUS program to analysis NP models of this degree of complexity. Therefore, part of my ongoing work will be dedicated to developing the DISCUS code in order to establish a complete model of the whole FePt-surfactant system. Furthermore, on obtaining results of higher statistical data from the next round of Nimrod beamtime, the NP-surfactant model can be refined using DIFFEV.

8.5 Collaboration: High Energy XRD-PDF Analysis and Modelling

Valeri Petkov has played an important role in developing the field of PDF analysis of NP alloys [Petkov et al., 2012]. Sample AM01 was sent to Valeri in order to obtain complementary high energy XRD data on these NPs. Valeri Petkov et. al, acquired x-ray diffraction measurements of these two samples, utilising the high energy x-rays of the 34-ID-C beamline (E = 115 keV, wavelength of 0.108Åand a Q = 10 $\AA^{-1}$), at the Advanced Photon Source (APS), Chicago.

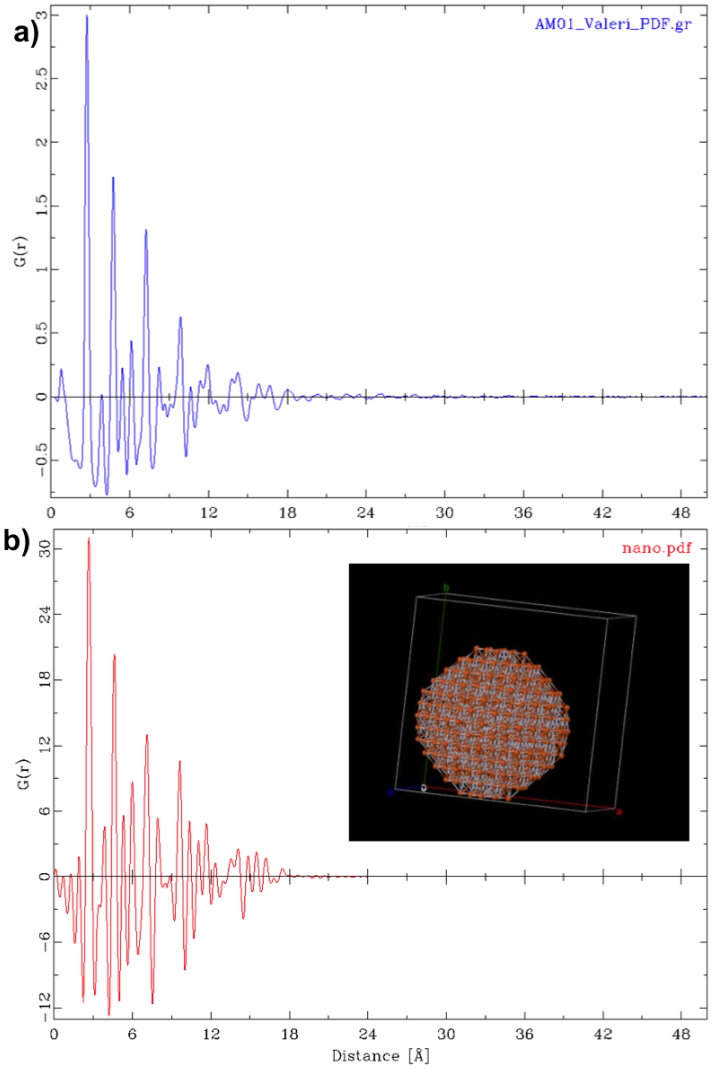

Figure 8.5: *XRD-PDFs of a) sample AM01 FePt NP samples and b) calculated PDF and 3D model of a 20 Årandomly disordered Fe_50Pt_50 NPs with a total of 270 atoms*

The resultant PDF of the diffraction pattern data acquired from the 20ÅNP sample in Figure 8.5 (a) corresponds well with the PDF from the 3D model of the FePt NPs in Figure 8.5(b) created with the same NP size and instrumental parameters.

8.6 Conclusion: Nanoparticle Modelling

The 3D NP models were created with the instrumental parameters defined within the PDF macros in order to obtain a model that was the closest representation of the NPs that were analysed in the neutron diffraction measurements.

The results from the calculated PDFs of the 3D models of 20Åand 40Åspherical NPs demonstrated the size effects of the NP on the PDF. Randomly disordered structures of FePt NPs were successfully modelled and NN distances and surface sites for future ligand attachment were identified. Core-shell structures (FePt@Pt) of FePt NPs were also successfully modelled. At the time of print NPs of SRO were in the process of being modelled. Determining the effect that the atomic structural arrangement in a NP have on the PDF model is part of this ongoing investigation. Complementary high energy XRD data was obtained from Sample AM01, 20ÅFePt NPs in collaboration with Valeri Petkov, and a 3D model and calculated PDF was created on the basis of the experimental data acquired.

In order to create a model that is the best representative of the NP system, more information is required such as the composition of the NPs. Thus both samples AM01 and AM06 have been sent off for Inductively coupled plasma atomic emission spectroscopy,ICP-AES, composition analysis. Also, NMR analysis of the NPs will provide an insight into the ligand ratio of surfactants on the surface of the NPs. In order to obtain a more accurate PDF model of the NP surfactant systems, can be obtained by taking an ensemble average of about 30 NP models and calculate the PDF. These improvements and refinements of the calculated models with the experimental PDFs will be explored in the next phase of this work utilising the capabilities of the DIFFUSE program.

Chapter 9

EngD Future Plan

9.1 Round 2 of Neutron Diffraction Experiments

The solvent effect on the dispersion of NPs has been reported as a result of studies using Scanning Electron Microscopy (SEM), but the structural effect the solvent has on the surfactant and the aggregation of the NPs, to the best of our knowledge, is yet to be established. Therefore, this continuing investigation aims to reveal the effect the solvent has on the short range structure and morphology of the surfactant, which arise from the chemical nature of the solvent.

The aim is to utilise Nimrod further in the next round of scheduled beamtime for effective analysis of the solvent and the surrounding atom-atom surfactant. As learned from the previous round, it is necessary to up-scale the synthesis to obtain a 1 g batch of NPs from each synthesis. In order to synthesise such a large batch of NPs economically (as deuterated surfactants are expensive), the molarity of the surfactant has been downsized by a third whilst keeping the ratio and the molarity of the precursors the same. This will not affect the size of the NPs as the synthesis procedure will remain the same, the only difference being there will be no excess surfactant. It is intended to employ H/D isotopic substitutions with specifically deuterated surfactants and solvent matrix, as outlined in Table 9.1. Additionally, we will do two contrast-matched experiments: firstly, matching the scattering length density (scattering per unit volume, b) of the surfactant layer to scattering length density of the solvent; so all we will see is the NP core and secondly, we will match the scattering length density of the NP core (calculated using the TEM-EDX results of the composition) to the scattering length density of the solvent, so all we will see is the surfactant layer.

The specifically deuterated/hydrogenated NPs will be dispersed and suspended in a deuterated long chain hydrocarbon solvent wax, such as eicosane C_nH_{2n+2}. The solvent wax melts at T 36 ° C, and is solid at room temperature. It is therefore highly effective for suspension of the NPs, and as a solvent matrix. The NP solutions will be dispersed in the solvent and sealed into our newly designed aluminium sample cans, which have the central square mould of the following dimensions: sample can 1: 4 x 20 x 20 mm = 0.8 cc = 0.622 g eicosane; and sample can 2: 2 x 20 x 20 mm = 1.6 cc = 1.245 g eicosane.

This mould will be where the NP-solvent suspension will be set as illustrated in Figure 9.2.

Substitutions	NP-surfactant	
Solvent	OA	HDA
1) D	H	H
2) H	D	D
3) D	D	D
4) H/D	D	D
5) D	D	H
6) D	H	D
Contrast match	7) $b_{surfactant} = b_{solvent}$	8) $b_{NP} = b_{solvent}$

Figure 9.1: *Proposed Experimental H/D Isotopic Substitutions, HDA: hexadecylamine, OA: oleic acid, H: hydrogenated, D: deuterated*

Figure 9.2: *Newly designed aluminium sample cans with central square mould cut out and eicosane wax dispensed within cut-out (where the NP sample will also be suspended)*

These two sample cans of different dimensions were designed to test which would be most suited, when accounting for the addition of 1 g batch of NPs into the eicosane solvent. This exposed sample is beneficial for neutron diffraction measurements, as there will be no requirement to subtract any background interference due to the can. This frame will then be attached to the standard NIMROD sample changer. The neutron diffraction data will enable PDFs of much higher resolution than is possible from an x-ray PDF. From PDF analysis of the substitutions we will refine real space structural models of the different NP-surfactant - solvent systems using a new combined modelling system.

The combination of neutron PDFs attained from the different isotopic substitution reactions will be analysed through 2nd order difference measurements to acquire a range of correlations within the system. The DIFFUSE package has been already used to create a 20 ÅFePt NP, with fcc structure of different ordering, and will be further applied to attach organic surfactants. This upcoming investigation will call for new modelling developments to further the data analysis code, as, although DISCUS is highly effective in the modelling of NP systems in vacuum, it is still to be adapted to interpret the effect of the surrounding solvent. Additionally, the program by Soper A.K., Empirical Potential Structure Refinement (EPSR), has long been developed and established to interpret solvent structure and behaviour by building 3D structural models. Therefore, for full data analysis of the whole system, we intend to work in collaboration with David Keen and Tristan Youngs in order to combine the NP- surfactant modelling of the DISCUS package, and the solvent structural determination of the EPSR package.

9.2 JAIST: Transmission Electron Tomography

Finally, a direct experimental observation of the 3D behaviour of FePt NPs, can be carried out through advanced Electron Tomography techniques. However, due to restricted access to this equipment and also the lack of capabilities of the equipment and software available locally in the UK, I have applied for a scholarship further afield, with Shinya Maenosano, a professor at the JAIST School of Materials Science. This scholarship has been applied for through the Summer Program Japan Scheme and runs over the course of two months in June to August '13. Shinya Maenosano is a leading contributor in this field of research and has the expertise and equipment available for this tomography investigation to be feasible.

Tomography, using aberration corrected electron microscopy is the optimum method to do so, as it provides quantitative real space information about the internal structure.

The work of Scott et al., is dedicated to the development of the electron tomography technique and has developed a new centre of mass alignment method and iterative reconstruction algorithm enabling an accurate reconstruction of a 10 nm NP gold NP at a resolution of 2.4 Åwith a low discrepancy of 6.7 % between the calculated and experimental [Scott et al., 2012]. What is interesting, analysing the FePt alloy, is that as HAADF-STEM is chemically sensitive, high contrast projections will be obtained between the lighter Fe (Z=26), and the heavier Pt (Z=78) enabling Fe and Pt to be easily distinguished. For the analysis, I will supply the FePt NPs in the fcc phase, which have already been analysed using neutron diffraction in the ongoing work. The 20 Å(2nm) NPs will be supported on Si membrane frames and a single NP will be isolated and analysed using HAADF-STEM tomography.

The intended outcome of the proposed research at JAIST is to successfully build a 3D quantitative reconstruction of the internal structure of FePt NPs, by isolating a single FePt NP and taking a collation of electron micrographs over a tilt series. The reconstruction would provide structural information on the 3D periodical arrangements of Fe and Pt, and identify the presence of any vacancies or defects within the NP. Also, the morphology will be defined through the quantification of the relative of the crystallographic facets present on the particle surface. It is hoped, through analysis of the data obtained from the TEM tomography, that a relation between the compositional modulations and nanocrsystal morphology will be successfully identified. The results aim to provide complementary information that will allow a direct comparison of the 3D NP model created in DISCUS (from the neutron PDF data) to the direct experimental structure obtained using this new tomography method.

Acknowledgements

I would like to thank my supervisor Prof. Ian Robinson from the London Centre for Nanotechnology for his continued support, advice and ideas. Thank you to Ana Estandarte from my group, for working together with the synthesis in preparation for the neutron diffraction beamtime. I would also like to acknowledge the funding I have received from the UCL Molecular Modelling and Materials Science Doctorate Training Centre. Finally, I would like to thank my industrial sponsor, Diamond Light Source, for the additional financial support.

Appendices

.1 Apparatus

The Schlenk line apparatus was set up as detailed in Figure 3, for the synthesis of the FePt NPs. This apparatus is required to reduce any presence of moisture and oxygen during the synthesis procedure.

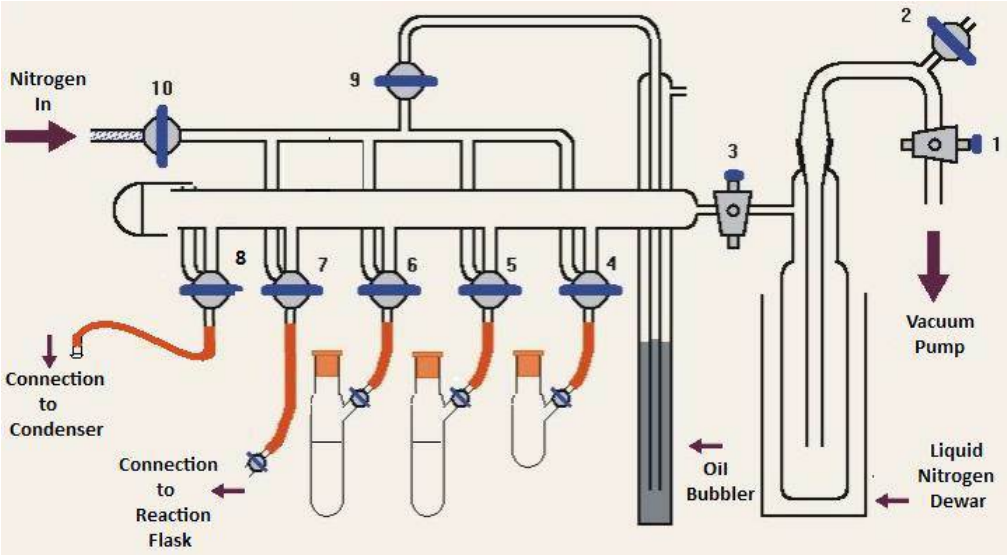

Figure 3: *Schematic of Schlenk line set-up with numbered connector taps [Fridgen, T.D., 2006]*

Taps 1 and 2 control the vacuum system, which is run through a liquid nitrogen dewar, which is a precautionary measure acting as a cold trap condensing any liquid that may have escaped into the system. Once the vacuum had been set to atmospheric pressure the trap was placed in the liquid nitrogen dewar and the vacuum pump was turned on. A vacuum could then be attained in the system by opening tap 3. Taps 4-8 could then be opened to vacuum by turning them horizontally. The other side of the tap would open to the N_2 supply. The N_2 is supplied to the system via tap 10 and tap 9 is always open when on to indicate the strength of the N_2 flow.

Tap 4 is the N_2 supply system for purging the gas tight syringes with N_2. Before use, tap 4 opened and the bottle connected is filled with N_2 whilst a needle inserted allows any air inside to be pushed out. Taps 5 and 6 are for the degassed dioctyl ether and ethanol which are supplied with N_2 on removal of any solvents. Tap 7 is connected to the side neck of the reaction flask and Tap 8 is connected to the condenser of the reaction flask as indicated in Figure 4. This three necked round-bottomed flask was used for the synthesis reaction.

The left neck opening was used to input the initial metal precursors and the liquid reagents (when sealed with a septum) and for the insertion of the temperature probe. The centre neck was used for the attachment of the condenser system, which is connected to tube 8 (Figure 3). The condenser is required to prevent any reaction gases from escaping out of the flask into the Schlenk line. The right side neck was used to attach connector tube 7, which can be used to vacuum the flask or to fill it with N_2 where required. The flask was based on top of a heating mantle, which has a variable temperature supply (knob 11) up to 300 °C. The mantle is connected to a temperature probe which is used to monitor the temperature of the reaction.

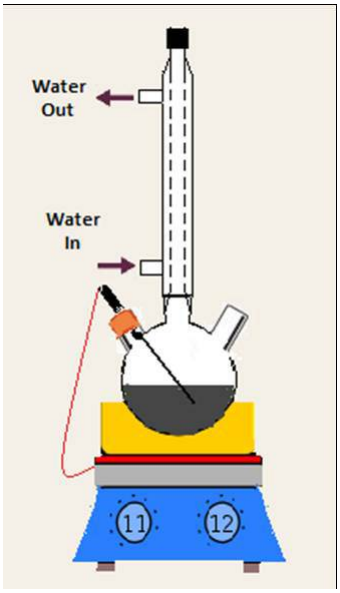

Figure 4: *Schematic of round-bottomed reaction flask on heating mantle,with a middle neck connection for the condenser and right neck connection for the flask arm*

The variable magnetic stirrer (knob 12) was kept at a constant 500 rpm for each reaction, it can however be varied to slow down or increase the rate of stirring depending on the size of NP required [Kong et al., 2011].

.2 Macros

.3 Macros cell used in FePt NP modelling

title FePt
spcgr Fm-3m
cell 3.779000 3.779000 3.779000 90.000000 90.000000 90.000000
atoms
FE 0.0000000 0.0000000 0.0000000 0.000000
PT 0.0000000 0.0000000 0.0000000 0.000000

Bibliography

[A.K., 2009] A.K., S. (2009). Inelasticity corrections for time-of-flight and fixed wavelength neutron diffraction experiments. *Molecular Physics*, 107(16):1667–1684.

[A.K., 2011] A.K., S. (2011). Gudrunn and gudrunx: programs for correcting raw neutron and x-ray diffraction data to differential scattering cross section. *Technical Report RAL*, page 4915.

[Bowron et al., 2010] Bowron, D. T., Soper, A. K., Jones, K., Ansell, S., Birch, S., Norris, J., Perrott, L., Riedel, D., Rhodes, N. J., Wakefield, S. R., Botti, A., Ricci, M.-A., Grazzi, F., and Zoppi, M. (2010). Nimrod: The near and intermediate range order diffractometer of the isis second target station. *Review of Scientific Instruments*, 81(3):033905.

[Calatayud et al., 2013] Calatayud, D. G., Jardiel, T., Rodrguez, M., Peiteado, M., Fernndez-Hevia, D., and Caballero, A. C. (2013). Soft solution fluorine-free synthesis of anatase nanoparticles with tailored morphology. *Ceramics International*, 39(2):1195 – 1202.

[Delalande et al., 2012] Delalande, M., Guinel, M. J. F., Allard, L. F., Delattre, A., Le Bris, R., Samson, Y., Bayle-Guillemaud, P., and Reiss, P. (2012). L10 Ordering of Ultrasmall FePt Nanoparticles Revealed by TEM In Situ Annealing. *The Journal of Physical Chemistry C*, 116(12):6866–6872.

[Hergt et al., 2006] Hergt, R., Dutz, S., Müller, R., and Zeisberger, M. (2006). Magnetic particle hyperthermia: nanoparticle magnetism and materials development for cancer therapy. *Journal of Physics: Condensed Matter*, 18(38):S2919–S2934.

[Jun et al., 2007] Jun, Y.-w., Choi, J.-s., and Cheon, J. (2007). Heterostructured magnetic nanoparticles: their versatility and high performance capabilities. *Chem. Commun.*, 0:1203–1214.

[Kong et al., 2011] Kong, J.-Z., Gong, Y.-P., Li, X.-F., Li, A.-D., Zhang, J.-L., Yan, Q.-Y., and Wu, D. (2011). Magnetic properties of FePt nanoparticle assemblies embedded in atomic-layer-deposited Al2O3. *J. Mater. Chem.*, 21:5046–5050.

[Nguyen et al., 2006] Nguyen, H. L., Howard, L. E. M., Stinton, G. W., Giblin, S. R., Tanner, B. K., Terry, I., Hughes, A. K., Ross, I. M., Serres, A., and Evans, J. S. O. (2006). Synthesis of size-controlled fcc and fct fept nanoparticles. *Chemistry of Materials*, 18(26):6414–6424.

[Page et al., 2011] Page, K., Hood, T. C., Proffen, T., and Neder, R. B. (2011). Building and refining complete nanoparticle structures with total scattering data. *Journal of Applied Crystallography*, 44(2):327–336.

[Page et al., 2010] Page, K., Proffen, T., Niederberger, M., and Seshadri, R. (2010). Probing local dipoles and ligand structure in batio3 nanoparticles. *Chemistry of Materials*, 22(15):4386–4391.

[Petkov et al., 2012] Petkov, V., Wanjala, B. N., Loukrakpam, R., Luo, J., Yang, L., Zhong, C.-J., and Shastri, S. (2012). Ptau alloying at the nanoscale. *Nano Letters*, 12(8):4289–4299.

[Rong et al., 2006] Rong, C.-b., Li, D., Nandwana, V., Poudyal, N., Ding, Y., Wang, Z., Zeng, H., and Liu, J. (2006). Size-dependent chemical and magnetic ordering in l10-fept nanoparticles. *Advanced Materials*, 18(22):2984–2988.

[Saita and Maenosono, 2005] Saita, S. and Maenosono, S. (2005). Formation mechanism of fept nanoparticles synthesized via pyrolysis of iron(iii) ethoxide and platinum(ii) acetylacetonate. *Chemistry of Materials*, 17(26):6624–6634.

[Scott et al., 2012] Scott, M. C., Chen, C.-C., Mecklenburg, M., Zhu, C., Xu, R., Ercius, P., Dahmen, U., Regan, B. C., and Miao, J. (2012). Electron tomography at 2.4-ngstrm resolution. *Nature*, 483:444–447.

[Shukla et al., 2003] Shukla, N., Liu, C., Jones, P. M., and Weller, D. (2003). Ftir study of surfactant bonding to fept nanoparticles. *Journal of Magnetism and Magnetic Materials*, 266(12):178 – 184. ¡ce:title¿Proceedings of the 4th International Conference on Fine Particle Magnetism (ICFPM)¡/ce:title¿.

[Soper and Barney, 2011] Soper, A. K. and Barney, E. R. (2011). Extracting the pair distribution function from white-beam X-ray total scattering data. *Journal of Applied Crystallography*, 44(4):714–726.

[Suda et al., 2007] Suda, M., Nakagawa, M., Iyoda, T., and Einaga, Y. (2007). Reversible photoswitching of ferromagnetic fept nanoparticles at room temperature. *Journal of the American Chemical Society*, 129(17):5538–5543. PMID: 17411039.

[Sun, 2006] Sun, S. (2006). Recent advances in chemical synthesis, self-assembly, and applications of fept nanoparticles. *Advanced Materials*, 18(4):393–403.

[Turkevich J, 1951] Turkevich J, Stevenson PC, H. J. (1951). A study of the nucleation and growth processes in the synthesis of colloidal gold. *Discuss Faraday Soc.*, 11:5575.

[van Ewijk et al., 2002] van Ewijk, G. A., Vroege, G. J., and Philipse, A. P. (2002). Susceptibility measurements on a fractionated aggregate-free ferrofluid. *Journal of Physics: Condensed Matter*, 14(19):4915.

[Wipf, 2007] Wipf, P. (2007). *LaTeX: A Techniques for Handling Air-Sensitive Compounds.* Chem 1140.

[Young and Goodwin, 2011] Young, C. A. and Goodwin, A. L. (2011). Applications of pair distribution function methods to contemporary problems in materials chemistry. *J. Mater. Chem.*, 21:6464–6476.

[Rong et al., 2010] Rong, C.-B., Poudyal, N., and Liu, J. P. (2010). Eect of thermal fluctuations on magnetization reversal of l 1 0 fept nanoparticles. Journal of Physics D: Applied Physics, 43(49):495001.

[Saita and Maenosono, 2005c] Saita, S. and Maenosono, S. (2005c). Formation mechanism of fept nanoparticles synthesized via pyrolysis of iron(iii) ethoxide and platinum(ii) acetylacetonate. Chemistry of Materials, 17(26):66246634.

[Chen et al., 2007] Chen, J. S., Tan, C. Y., and Chow, G. M. (2007). Microstructure and direct ordering of fept nanoparticles produced by nanocluster beam technology. Nanotechnology, 18(43):435604.